Quantum Otto engine powered by critical XY-Γ chain

Anass Hminat [1], Abdallah Slaoui [1,2] Rachid Ahl Laamara,[1,2] and Amine Jaouadi [3]

[1] *LPHE-Modeling and Simulation, Faculty of Sciences, Mohammed V University in Rabat, Rabat, Morocco.*
[2] *Centre of Physics and Mathematics, CPM, Faculty of Sciences, Mohammed V University in Rabat, Rabat, Morocco.*
[3] *LyRIDS, ECE-Paris School of Engineering, 10 rue Sextius Michel, 75015 Paris - France*

(Dated: December 26, 2025)

We present a theoretical study of the thermodynamic properties of a four-stroke engine whose working medium is an XY quantum spin chain. The cycle alternates unitary strokes—realized via controlled modulations of a transverse magnetic field—with thermalization strokes produced by coupling the chain to thermal reservoirs at different temperatures. The open-system dynamics are treated within a thermodynamically consistent formalism based on a nonlocal Lindblad master equation. Depending on the choice of system parameters, the device exhibits four distinct operating regimes and can act either as a heat engine or as a refrigerator. Notably, we observe a marked improvement of the machine's performance in the vicinity of the quantum critical point. We also analyze the roles played by the off-diagonal coupling Γ and the anisotropy parameter γ, and discuss strategies to optimize the engine's figures of merit in both operational modes.

I. INTRODUCTION

Thermodynamics is a fundamental branch of physics devoted chiefly to the study of heat [1]. It has not only underpinned the design of internal combustion engines but also contributed to our understanding of the thermodynamic aspects of black holes. Technological progress has driven the miniaturization of components [2], placing many devices in regimes where quantum effects are non-negligible. In parallel, the rise of quantum technologies and the development of nanoscale systems that exchange heat and perform work have made it increasingly pertinent to examine these processes within a quantum-mechanical framework [3]. Despite the maturity of classical thermodynamics, its extension to quantum systems poses conceptual challenges and remains an active area of research. Early efforts to generalize the notions of heat and work to the quantum domain date back to the 1980s [4]. Only recently has a renewed interest in quantum thermal machines spurred prolific scientific advancements, starting with the groundbreaking proposal of the maser [5] as the first example of a quantum machine.A quantum thermal machine may be broadly characterised as a device composed of quantum subsystems that is able to perform work by evolving through an appropriate thermodynamic cycle [6]. A variety of proposals have explored few-body quantum machines based on classical cycles such as the Carnot [7, 8], Otto [9, 10], Stirling [11, 12], Brayton [13], and Diesel cycles [14]. Implementations and theoretical models have been investigated across several platforms, including particles in infinite potential wells [15], nuclear magnetic resonance systems [16], ultracold atomic setups [17], and relativistic scenarios [18, 19].

Nevertheless, the influence of many-body interactions on the thermodynamic performance of quantum machines remains incompletely understood [20–22]. Systems with long-range interactions present attractive opportunities for quantum technologies because of their enhanced robustness against external perturbations [23–25]. Such stability facilitates better control over dynamically generated excitations and helps mitigate their harmful effects. In particular, a dynamical phase transition is well defined when $\alpha < 1$ [26, 27], whereas for $\alpha > 1$ the sharp critical point broadens into a chaotic crossover region in which the dynamics and the long-time state become highly sensitive to system parameters. Employing many-body quantum systems as the working medium of thermal machines is a promising route to achieving a quantum advantage [28, 29], although it poses substantial analytical and numerical challenges; nonetheless, several preliminary studies have reported encouraging results [30–32]. Quantum criticality has been identified as a possible resource for improving engine performance [33–35], but the precise role of many-body interactions in determining the thermodynamic efficiency of quantum engines remains an open question. One of the main obstacles lies in the difficulty of solving the dynamics of these many-body systems [36–38]. In contrast to the more conventional modeling frameworks based on master equations incorporating Lindblad operators acting locally within the system's physical degrees of freedom [39–41], the present approach naturally accommodates stationary thermal states, thereby circumventing potential thermodynamic inconsistencies that may arise in local dissipative schemes [42, 43].

Quantum critical behaviour in $S = 1/2$ Ising systems has been experimentally established in several compounds, notably LiHoF4 [39], CoNb2O6 [40], and SrCo2V2O8 [41]. More recently, it has become apparent that the combined influence of spin–orbit coupling (SOC) and the crystalline electric field can stabilise a well-isolated Kramers doublet ground state [42], thereby producing strongly anisotropic $J_{\text{eff}} = 1/2$ moments that are naturally captured by a generalized 3×3 exchange tensor $J_{\beta\beta'}$ together with an anisotropic g-tensor [43]. In this context, off-diagonal exchange interactions—nontrivial manifestations of SOC—require careful treatment and are particularly pertinent in systems proposed to host spin-liquid phases [44]. Such symmetric off-diagonal couplings have been identified as central to a variety of magnetic phenomena, including weak ferromagnetism [45, 46], the emergence of spin-spiral textures [47], and the formation of skyrmion lattices [48]. Recently, symmetric off-diagonal terms commonly denoted Γ and Γ' have been shown to significantly affect candidate Kitaev materials such as α-RuCl3 [49–54], β-Li2IrO3 [55, 56], and A2IrO3 [57–59]. Despite extensive investigation, the microscopic consequences of these

off-diagonal couplings remain incompletely understood: they have been proposed to favour spin-liquid behaviour in diluted RuCl3 [60], while other studies suggest they may enhance the robustness of topological phases [52]. Owing to their rich and varied phenomenology, theoretical models that incorporate these interactions continue to provide a fruitful arena for further exploration [61].

The structure of this paper is as follows. In Section II, we first present and describe our XY-Γ chain model and discuss its critical behavior and the dynamic of the chain in the Otto cycle (see Fig.1). The Section III introduces the microscopic framework of a four-stroke Otto engine, with its working medium comprising a quantum XY spin chain interacting with two thermal reservoirs (see Fig.2). We explore the permissible operational mode regimes, which are markedly affected by the temperatures of the hot and cold reservoirs, the anisotropy parameter γ, and the Γ interaction strength Γ. Next, we will investigate the impact of reservoir temperatures on the performance of a quantum engine and the influence of spin interactions through variations in the chain size N. Furthermore, we will analyze the effect of anisotropy and Γ interaction on the dynamics and performance of the cycle, as well as the influence of quantum criticality. Section IV is dedicated to the study of the stability of the quantum heat engine and refrigerator through the analysis of the scaling factor for different thermal reservoir sizes, as well as the performance of our system for various anisotropies and the symmetric off-diagonal interaction, aiming at better optimization. We present our conclusions in Section V. Additional technical details are provided in the appendices, including the diagonalization procedure for the quantum XY-Γ chain (Appendix A- C), as well as on the modeling of thermal correlations and their behavior in the vicinity of the phase transition (Appendix D-E) and we will also see the probability of a nonadiabatic transition and LZSM problem in Appendix F.

II. XY GAMMA

The model considered in this paper is a one-dimensional spin-$\frac{1}{2}$ XY chain in a transverse field [62], supplemented by a generalized Γ interaction. This model, is solvable chain and one of the benchmark integrable models [63–65], serves as the working substance of our study, the Hamiltonian is given by

$$H = H_{XY} + H_{\Gamma}, \tag{1}$$

with

$$H_{XY} = -J\sum_{n=1}^{L}\Big[\Big(1+\frac{\delta}{2}\Big)\sigma_n^x\sigma_{n+1}^x+\Big(1-\frac{\delta}{2}\Big)\sigma_n^y\sigma_{n+1}^y\Big]-h\sum_{n=1}^{L}\sigma_n^z, \tag{2}$$

and

$$H_{\Gamma} = -\Gamma\sum_{n=1}^{L}\Big(\sigma_n^x\sigma_{n+1}^y+\gamma\,\sigma_n^y\sigma_{n+1}^x\Big), \tag{3}$$

where σ_i^{α} denote the standard Pauli matrices at site i, $\gamma \in [-1,1]$ is the parameter characterizing the anisotropy , the

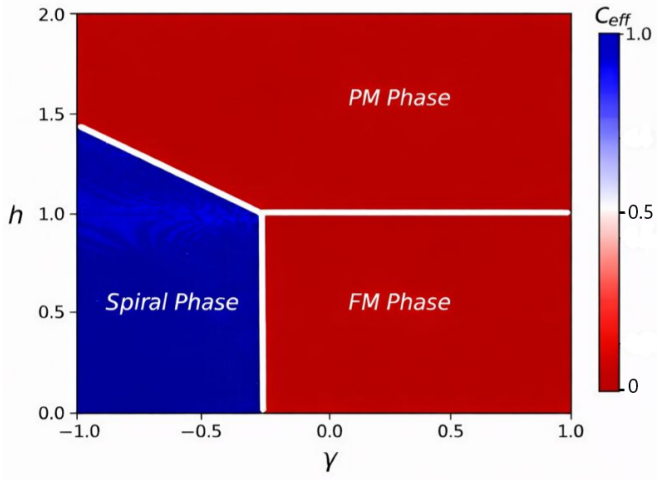

FIG. 1: We present the effective central charge c_{eff}, determined through fitting procedures applied to $S_{L/2}(L)$, plotted against the transverse field strength h and the anisotropy γ. Along the phase boundary dividing the ferromagnetic (FM) and paramagnetic (PM) regimes, a conformal field theory without gap is clearly visible, manifesting an effective central charge of $c_{\text{eff}} = 1/2$. The other transition lines, however, display a null effective central charge. Throughout the interiors of both the FM and PM phases, this quantity remains zero, whereas in the spiral phase it adopts the value $c_{\text{eff}} = 1$. These findings are obtained for the parameter set $J = 1.0$, $\delta = 0.6$, and $\Gamma = 0.6$.Finally, we note that the residual fluctuations observed in the spiral phase are attributable to finite-size effects and will be suppressed by increasing the system size , vanishing in the thermodynamic limit $L \to \infty$.

Hamiltonian describes a generalised XY spin chain, with $\gamma = \pm 1$ recovering the transverse-field Ising model and $\gamma = 0$ corresponding to the rotationally invariant XX chain. Here, J denotes the overall ferromagnetic coupling, δ quantifies the anisotropy in the spin-exchange interaction, and h represents the intensity of the applied uniform transverse field. The parameter Γ controls the magnitude of additional off-diagonal exchange contributions, while γ determines their relative weighting with respect to the standard XY terms. The system consists of N lattice sites in total. The ground-state phase structure features three distinct regimes, as depicted in Fig.1.:

- **Ferromagnetic (FM) phase**, which is gapped,
- **Paramagnetic (PM) phase**, which is also gapped,
- **Spiral phase**, which is gapless and characterized by quasi-long-range order.

The identification of critical behaviour relies on examining the time evolution of entanglement entropy after a sudden global quench performed at zero temperature, following the methodology described in Ref [66]. For this purpose, we partition the quantum system into two subsystems A and B such that the total Hilbert space reads $\mathcal{H} = \mathcal{H}_A \otimes \mathcal{H}_B$,

with the initial state being a pure many-body wave function $\rho = |\Psi_0\rangle\langle\Psi_0|$. The von Neumann entropies characterising the reduced states of these two partitions,

$$S_{A/B} = -\mathrm{Tr}\big(\rho_{A/B}\ln\rho_{A/B}\big)\,,$$

and measuring the bipartite quantum correlations, where the reduced density operators are $\rho_{A/B} = \mathrm{Tr}_{B/A}\rho$ [67]. In what follows we take $|\Psi_0\rangle$ to be the ground state of the pre-quench Hamiltonian. At time $t = 0$ a system parameter is abruptly changed to a new value and the state subsequently evolves under the post-quench Hamiltonian. For an infinite chain of free spinless fermions, the entanglement entropy of a contiguous block A containing ℓ sites can be obtained from the spectrum of the correlation matrix. Denoting the entropy by $S_\ell(t)$ one has

$$S_\ell(t) \;=\; -\sum_{x=1}^{2\ell}\lambda_x\ln\lambda_x, \tag{4}$$

where $\{\lambda_x\}$ are the eigenvalues of the $2\ell\times 2\ell$ matrix

$$\mathbf{M} \;=\; \begin{pmatrix}\mathbf{\Theta} & \mathbf{T}\\ \mathbf{T}^\dagger & \mathbf{R}\end{pmatrix}. \tag{5}$$

Here the $\ell\times\ell$ blocks are constructed from two-point correlators,

$$\Theta_{nm} = \langle c_n^\dagger c_m\rangle, \qquad T_{nm} = \langle c_n^\dagger c_m^\dagger\rangle, \qquad R_{nm} = \delta_{nm} - \Theta_{mn},$$

with $c_n^\dagger$ (c_n) the fermionic creation (annihilation) operators. It is well established for one-dimensional integrable models that entanglement spreads ballistically after a global quench [68]: the entropy growth scales with the boundary of subsystem A rather than its volume, in agreement with the so-called *area law*. Ground states of noncritical, short-range Hamiltonians with finite correlation length therefore display a saturation of entanglement entropy for large subsystems [69]. At a quantum critical point, however, an interval of size $L/2$ exhibits a logarithmic violation of the strict area law. In that case the entropy behaves as

$$S_{L/2}(L) = \frac{c_{\mathrm{eff}}}{3}\,\ln L + b, \tag{6}$$

where c_{eff} denotes the effective central charge and b is a nonuniversal constant [70, 71]. More precisely, we found that the FM and PM phases are separated by a critical point at $h_{c1} = 1$ (for $\gamma > \delta^2/(4\Gamma^2)$), while the spiral phase emerges for $h \le 1$ and is delineated by phase transitions at $\gamma_{c1} = \delta^2/(4\Gamma^2)$ (from the FM phase) and at $h_{c2} = \sqrt{1-\delta^2-4\Gamma^2\gamma}$ (from the PM phase, for $\gamma < \delta^2/(4\Gamma^2)$).

The system under consideration is described by a Hamiltonian featuring the spin-1/2 Pauli operators σ_j^α, where j denotes the j-th site and $\alpha = x, y, z$ specifies the Cartesian components. The coupling constant J may take positive values $J > 0$. We consider periodic boundary conditions with an even number of sites. For the purposes of this study, we adopt $J = 1$ as the reference energy scale and work in natural units where $\hbar = k_B = 1$. The exact diagonalization of the Hamiltonian is readily achieved by reformulating it in terms of independent fermionic degrees of freedom, thereby obtaining the entire eigenvalue spectrum. It is a standard result [72] that the non-interacting fermionic equivalent of the XY model emerges from the successive application of the Jordan-Wigner transformation and a Bogoliubov rotation in reciprocal space, leading to a fully separable form of the Hamiltonian.The dynamic is modeled by nonlocal master equation chosen to model the interaction between the system and environment [73]. For the sake of generality, we now examine a broader setup involving N_B distinct and independent thermal baths, each maintained at its respective temperature T_n, where the index n runs over the set $\{1,\ldots,N_B\}$ to identify individual reservoirs. The Hamiltonian describing this setup reads:

$$\hat{H}_{\text{env}} = \sum_{n=1}^{N_B}\int dk\,\varepsilon_n(k)\hat{c}_n^\dagger(k)\hat{c}_n(k),$$

with $\varepsilon_n(k) \ge 0$ and $\hat{c}_n(k)$, $\hat{c}_n^\dagger(k)$ being fermionic annihilation and creation operators. Given the mutual independence of the N_B reservoirs, the reduced density matrix associated with the entire environment takes on a product form.

$$\rho_{\text{env}} = \bigotimes_{n=1}^{N_B}\rho_{\text{bath}}^{(n)},$$

with $\rho_{\text{bath}}^{(n)}$ representing the canonical density matrix of the nth fermionic reservoir maintained at temperature T_n. For each reservoir n, we consider it coupled to p selected lattice sites of the system, the indices of which form the set I_n. The system-environment coupling is modelled through a quadratic interaction Hamiltonian that possesses a separable, factorized form.

$$\hat{H}_{\text{int}} = \sum_{n=1}^{N_B}\sum_{p\in I_n}\int dk\,g_n(k)\left(\hat{b}_p+\hat{b}_p^\dagger\right)\left(\hat{c}_n(k)+\hat{c}_n^\dagger(k)\right),$$

where $\hat{b}_p^{(\dagger)}$ and $\hat{b}_p^{(\dagger)}$ are the fermionic operators of the system. With $g_n(k)$ characterizing the magnitude of the coupling linking the kth excitation mode of the nth thermal reservoir to the designated system sites $p \in I_n$. It can be written in a factorized form

$$\hat{H}_{\text{int}} = \sum_{n=1}^{N_B}\hat{O}_n\otimes\hat{R}_n,$$

by defining

$$\hat{O}_n = \sum_{p\in I_n}(\hat{b}_p+\hat{b}_p^\dagger), \quad \text{and} \quad \hat{R}_n = \int \mathrm{d}k\,g_n(k)\left[\hat{c}_n(k)+\hat{c}_n^\dagger(k)\right].$$

Let's introduce the density of states associated with the nth bath:

$$J_n(\omega) \equiv \pi\int \mathrm{d}k\,|g_n(k)|^2\delta\left[\omega-\varepsilon_n(k)\right]. \tag{B.4}$$

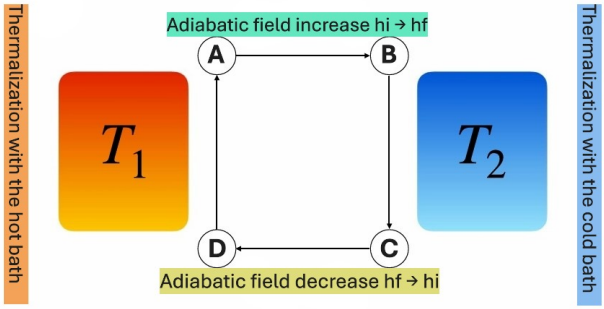

FIG. 2: Diagram illustrating the XY-Γ quantum Otto engine, which encompasses two adiabatic processes and two equilibration intervals. In the transition (A → B), the setup experiences adiabatic transformation as the perpendicular magnetic field is elevated from h_i to h_f. Next, during the interval (B → C), equilibrium is achieved with the low-temperature bath at T_c. The subsequent adiabatic reversal (C → D) returns the field to h_i, before equilibration occurs with the high-temperature bath at T_h in the final interval (D → A).

Under the assumption that the baths have a very large bandwidth compared to the frequencies of the system, we can approximate $J_n(\omega) \approx J_n$. Tracing out all the environmental degrees of freedom and imposing the Born–Markov approximation for the baths (for more details consult [10] Appendix B).It is possible to derive a microscopic Lindblad master equation:

$$\frac{d}{dt}\rho_{\rm sys}(t) = -i[\hat{H}_{\rm sys}, \rho_{\rm sys}] + D[\rho_{\rm sys}],$$

with

$$D[\rho_{\rm sys}] = \sum_{n,k} \gamma_{nk} \Bigg[(1 - f_n(\omega_k)) \left(\frac{1}{2}\hat{b}_k \rho_{\rm sys} \hat{b}_k^\dagger - \frac{1}{2}\{\hat{b}_k^\dagger \hat{b}_k, \rho_{\rm sys}\} \right) + f_n(\omega_k) \left(\frac{1}{2}\hat{b}_k^\dagger \rho_{\rm sys} \hat{b}_k - \frac{1}{2}\{\hat{b}_k \hat{b}_k^\dagger, \rho_{\rm sys}\} \right) \Bigg], \tag{7}$$

where the $\{\hat{b}_k, \hat{b}_k^\dagger\}$ jump operators are the fermionic Bogoliubov quasiparticles.The operators are local in the energy eigenbasis and nonlocal in the sites, giving rise to a global master equation [73].Under the assumption of no degeneracies in the spectrum , equation can be used to obtain an analytic expression for the time evolution of the correlation functions. Defining

$$\tilde{f}_k = \frac{\sum_n \gamma_{nk} f_n(\omega_k)}{\sum_n \gamma_{nk}} \quad \text{with} \quad f_n(\omega_k) = \frac{1}{1 + e^{\omega_k / T_n}},$$

we have

$$\langle \hat{b}_k^\dagger \hat{b}_k \rangle_t = \tilde{f}_k \left(1 - e^{-2 \sum_n \gamma_{nk} t} \right) + \langle \hat{b}_k^\dagger \hat{b}_k \rangle_0 e^{-2 \sum_n \gamma_{nk} t}.$$

Then:

$$\langle E_i \rangle = \sum_k \omega_{k,i} \left(\langle b_k^\dagger b_k \rangle - \frac{1}{2} \right). \tag{8}$$

III. THE QUANTUM OTTO CYCLE

In the present study, we propose a fully microscopic realisation of a four-stroke quantum Otto cycle, in which the working medium is a quantum XY spin chain interacting with two independent thermal baths. We further explore the extent to which proximity to quantum critical points can affect key performance characteristics, focusing primarily on operation as a heat engine and as a refrigerator. At the start of each stroke of the cycle (corresponding to points A, B, C, and D in Fig. 2), the state of the working fluid together with its average internal energy is characterised as detailed below:

$$\rho_A = \frac{e^{-H_A/T_A}}{Z_A}, \qquad \langle \hat{H}(t_i) \rangle_{\rho_A} = \mathrm{Tr}\big(\rho_A H_A\big), \tag{9a}$$

$$\rho_B = U\, \rho_A\, U^\dagger, \qquad \langle \hat{H}(t_f) \rangle_{\rho_B} = \mathrm{Tr}\big(\rho_B H_B\big), \tag{9b}$$

$$\rho_C = \frac{e^{-H_B/T_C}}{Z_B}, \qquad \langle \hat{H}(t_i) \rangle_{\rho_C} = \mathrm{Tr}\big(\rho_C H_B\big), \tag{9c}$$

$$\rho_D = U'\, \rho_C\, U'^\dagger, \qquad \langle \hat{H}(t_f) \rangle_{\rho_D} = \mathrm{Tr}\big(\rho_D H_A\big), \tag{9d}$$

We assume that during the unitary strokes the control parameter h varies linearly in time. In particular the protocol for the first (A→B) stroke is taken as

$$h(t) = h_i + \delta\, t, \qquad t \in [0, \tau], \tag{10}$$

with sweep rate $\delta = (h_f - h_i)/\tau$. The third (C→D) stroke is implemented by the time-reversed ramp

$$h'(t) = h_f - \delta\, t, \qquad t \in [0, \tau] \tag{11}$$

The corresponding unitary evolutions are the time-ordered exponentials

$$U = \mathcal{T} \exp\Big(-i \int_0^\tau dt\, H\big[h(t)\big] \Big), \tag{12}$$

$$U' = \mathcal{T} \exp\Big(-i \int_0^\tau dt\, H\big[h'(t)\big] \Big), \tag{13}$$

where $\mathcal{T}$ denotes time-ordering. During the second and fourth strokes the external driving is switched off and the system is coupled to the reservoirs; in these thermalisation strokes the system relaxes to the Gibbs states, at the respective temperatures T_1, T_2. We assume $h_i < h_f$ with $\delta h \equiv h_f - h_i = 0.5$ (see Fig.2 for details):

(a) $A \to B$**: Adiabatic ramp of the transverse field;** During this isolated stroke the transverse magnetic field is increased linearly from h_i to h_f over a duration τ, while the working medium remains decoupled from the thermal reservoirs , and the process is assumed adiabatic (no heat exchange with the baths).

$$h(t) = h_i + \frac{h_f - h_i}{\tau} t, \quad t \in \left[0, \frac{h_f - h_i}{\tau}\right]$$

(b) $B \to C$**: Thermalization with the cold bath;** The Hamiltonian $\hat{H}(t_f)$ is held fixed while the system is coupled to a cold reservoir at temperature T_c. The working medium is left to relax until it reaches the corresponding thermal state .

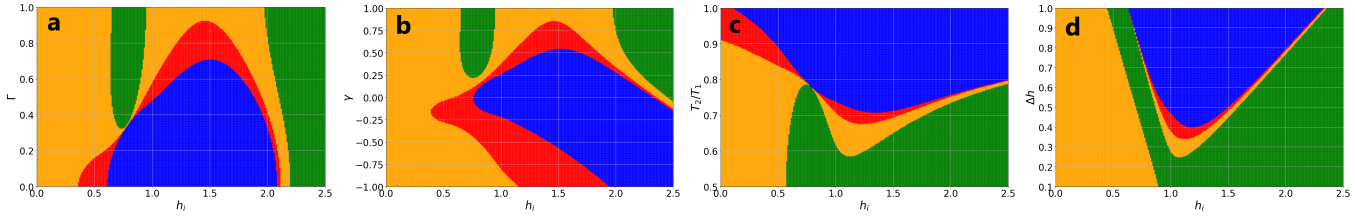

FIG. 3: Operating regimes of the quantum Otto engine. Panel (a) displays results in the $\Gamma - h_i$ plane for $T_h = 1.0$, $T_c = 0.75$ and $\Gamma \in [0, 1]$. Panel (b) shows the $\gamma - h_i$ plane for the same temperatures with $\gamma \in [-1, 1]$. Panel (c) gives the $T_c/T_h - h_i$ dependence as the ratio T_c/T_h is varied from 0.5 to 1 while Γ is held at 0. Panel (d) reports how the behavior changes when δh is swept from 0 to 1 (note that panels (a)–(c) were produced with $\delta h = 0.5$). The color legend marks four operational classes: accelerator (orange), heater (red), heat engine (green), and refrigerator (blue).

(c) $C \to D$**: Adiabatic ramp-down of the transverse field**
The working medium is isolated from the baths and the transverse field is decreased linearly from h_f back to h_i over a duration τ' , the process being assumed adiabatic (no heat exchange with the reservoirs).

$$h(t) = h_f - \frac{h_f - h_i}{\tau} t, \quad t \in \left[0, \frac{h_f - h_i}{\tau}\right]$$

(d) $D \to A$**: Thermalization with the hot bath;**
The Hamiltonian $\hat{H}(t_i)$ is kept constant and the system is coupled to the hot reservoir at temperature T_h until it returns to the initial thermal state.

In the following, we denote by $Q_{c(h)}$ the heat exchanged during thermalization with the cold (hot) reservoir, adopting the sign convention $Q_{c(h)} > 0$ when heat is absorbed by the system. Let ρ_α be the density matrix of the system at the points $\alpha \in \{A, B, C, D\}$. Then,

$$Q_c = \langle \hat{H}(t_f) \rangle_{\rho_C} - \langle \hat{H}(t_f) \rangle_{\rho_B}, \tag{14}$$

$$Q_h = \langle \hat{H}(t_i) \rangle_{\rho_A} - \langle \hat{H}(t_i) \rangle_{\rho_D}. \tag{15}$$

In particular, knowledge of the system's internal energy at the four cycle points A, B, C, D is sufficient to fully characterize its thermodynamic properties. Consider the limit of an infinitely slow cycle, $\delta \to 0$ (equivalently $\tau \to \infty$). In this regime—hereafter referred to as *adiabatic*—the unitary evolution is sufficiently slow for the adiabatic theorem to apply, so that transitions between distinct instantaneous eigenstates of the Hamiltonian are suppressed. The performance of a heat engine is characterized by two key metrics: the work output W and the efficiency η, where the efficiency is given by the ratio of work produced to heat absorbed. The second law of thermodynamics imposes an upper limit on the efficiency, known as the Carnot efficiency:

$$\eta = W/Q_h \quad \text{and} \quad \eta \leq \eta_C = 1 - \frac{T_c}{T_h}. \tag{16}$$

The work performed by the system during the adiabatic phase:

$$W_{i \to f} = -\int_{t_i}^{t_f} dt \, \langle \frac{d\hat{H}(t)}{dt} \rangle_{\rho(t)} = \langle \hat{H}(t_f) \rangle_{\rho_i} - \langle \hat{H}(t_f) \rangle_{\rho_f}.$$

This analysis can be readily adapted to parameter regimes where the engine functions as a refrigerator. In such cases, the key quantities are the heat Q_c removed from the cold reservoir and the coefficient of performance (COP) of a refrigerator quantifies its efficiency by measuring the ratio of heat extracted from the cold reservoir to the work input required to achieve this transfer due to the second law, is bounded by the Carnot COP:

$$\eta_R = \frac{Q_c}{|W|} \quad \text{and} \quad \eta_R \leq \eta_{R_C} = \frac{T_c}{T_h - T_c} \tag{17}$$

Introduce the transition probability $1 - P_k$, defined as the probability of a nonadiabatic transition between the energy levels of the k-th mode occurring during the unitary stroke of the cycle.For any fixed finite N, one can choose the driving duration large enough that the evolution becomes adiabatic; in this limit nonadiabatic transitions are suppressed and we may take $P_k = 1$ (see Appendix F and [126] for more details) .Within a Landau–Zener framework one expects this effect to be relevant when the quench velocity scales like $\delta \sim \Delta^2$ [128]. Conversely, if the quench is either too fast (approaching the sudden-quench limit) or too slow (approaching the adiabatic limit) relative to the gap, the dynamics become insensitive to the gap closure and the associated critical enhancement is suppressed [129] .

A. Fonctionement mode

We commence by examining the operational modes attainable by the Otto cycle described earlier (see Fig.3). Through the integration of the Clausius inequality with the first law of thermodynamics, the computational findings unequivocally illustrate that the engine possesses the capacity to function across all four thermodynamic regimes , heat engine (green), refrigerator (blue), heater (red) and accelerator (orange) mode with each occupying significant regions in the parameter space [74]:

- **Refrigerator (R)**: In this regime the device consumes energy to pump heat from the cold reservoir into the hot reservoir; accordingly $Q_c > 0$, $Q_h < 0$, and $W < 0$.

- **Accelerator (A)**: In this mode the device absorbs energy while assisting the transfer of heat from the hot reservoir to the cold reservoir; accordingly i.e., $Q_c < 0$, $Q_h > 0$, and $W < 0$.

- **Heat engine (E)**: Operating as a heat engine, the device converts heat drawn from the hot reservoir into useful work; consequently, $Q_c < 0$, $Q_h > 0$, and $W > 0$.

- **Heater (H)**: In this mode the device consumes external energy and raises the temperatures of both reservoirs; accordingly , $Q_c < 0$, $Q_h < 0$, and $W < 0$.

Figure 3(a–d) presents phase diagrams of the XY-Γ Otto engine, illustrating how the device's operational regimes depend sensitively on the hot and cold reservoir temperatures, the anisotropy parameter γ, and the symmetric off-diagonal interaction interaction strength Γ. These quantities jointly determine the appearance and stability of distinct thermodynamic modes across the control-parameter space. All simulations reported below assume a quench amplitude $\delta h \equiv h_f - h_i = 0.5$, and the default system size N unless otherwise stated.

Panels (a) and (b) isolate the roles of the coupling Γ and the anisotropy γ, respectively. The γ term, entering effectively as a squared contribution, produces qualitatively similar behavior for positive and negative signs of Γ: regions characterized by heat-engine and accelerator operation appear both before and after the quantum critical point (see Fig. 3a), while refrigerator and heater regimes emerge at the critical field. In the vicinity of the transverse-field critical point the accelerator and engine domains proliferate on both sides of the transition, and the boundary separating these domains from heater and refrigerator behavior shifts abruptly with Γ and γ, signalling the underlying quantum phase transition. Anisotropy (Fig. 3b) enforces heater and refrigerator operation for negative and small values of γ, whereas larger γ produces a richer mixture of modes: engine and accelerator regions interchange near the phase boundary.

Panels (c) and (d) illustrate the influence of the temperature ratio T_c/T_h and the quench amplitude δh. Thermal effects are most pronounced close to the XY critical point $h_{\rm crit} = 1$, where the vanishing energy gap [75] renders quenches more dissipative and complicates coherent work extraction; this gives rise to a reentrant heat-engine region that is more prominent at $T_c/T_h = 0.5$ than at $T_c/T_h = 1.0$ (Fig. 3c). Denoting the temperature difference by $\Delta T \equiv T_h - T_c$, we find that large thermal gradients favor the engine regime, while reducing ΔT drives the system through intermediate accelerator and heater behaviors and ultimately into the refrigerator domain. Increasing the quench amplitude (Fig. 3d) displaces the left boundary of the heat-engine region toward lower transverse-field values and enlarges the refrigerator sector at lower T_c; the panels quantify how the engine and refrigerator boundaries evolve with δh for $N = 100$, $T_c = 0.75$, and $T_h = 1.0$.

In summary, the XY-Γ quantum Otto engine implemented on a finite Heisenberg spin chain exhibits a rich, tunable thermodynamic phase structure governed by γ, Γ, the temperature ratio T_c/T_h, and the quench amplitude δh. All four operational modes—heat engine, refrigerator, heater, and accelerator—occupy substantial regions of parameter space. Engine and accelerator regimes dominate near and beyond the critical point for intermediate values of γ and Γ, whereas refrigerator and heater modes tend to concentrate around $h_{\rm crit} = 1$, where quantum critical fluctuations suppress coherent work extraction. These results underscore the decisive roles of microscopic interactions, thermal gradients, and quench intensity in shaping the performance and control of quantum thermal machines.

B. Temperature influence

In this section we examine how reservoir temperatures influence the performance of both a quantum heat engine and a refrigerator, with thermodynamic observables plotted as functions of the initial transverse field h_i (see Fig. 4). For the engine calculations we set $N = 100$ and fix the hot-reservoir temperature at $T_h = 1.0$, while varying the cold temperature over the set $T_c \in \{0.15, 0.2, 0.3, 0.4, 0.45\}$. In finite-temperature systems situated near a quantum critical point one generally expects enhanced heat exchange and energy conversion: the specific heat diverges [116], permitting large heat transfer for modest temperature differences, and the magnetic susceptibility—quantifying the magnetization response to an applied field—also grows large close to criticality [75]. Since the work associated with changing the magnetic field is directly proportional to the magnetization [83], these thermodynamic divergences produce pronounced features in the engine's output.

Figures 4(a)–(b) display the work per spin W/N and the efficiency η as functions of h_i. As the cold-reservoir temperature decreases, the thermal gradient $\Delta T \equiv T_h - T_c$ increases, and enhances the population of critical modes , which amplifies the extracted work per cycle, wich yields a prominent peak in W/N near the critical field $h_{\rm crit} = 1$. This peak reflects the enhanced thermal and quantum fluctuations at the transition, where the effect appears as a pronounced growth of the correlation length ξ, leading to a stronger collective response [84]. Linking these quantities to the measured energy responses to reveal their influence on the system's energetic behavior. In practice, a large susceptibility means that a small variation in field or temperature causes a large variation in the stored energy. This is explained by the amplification of the heat capacity and susceptibilities near the critical point [85], these enhanced quantities enable larger energy exchanges, which in turn result in more efficient conversion into work.

The paramagnetic peak becomes increasingly dominant relative to the ferromagnetic feature as ΔT grows, and η exhibits a concomitant improvement with larger ΔT, attaining its maximum in the vicinity of the critical point where amplified heat capacity facilitates more efficient adiabatic exchanges.

Where quasi-particle excitations populate differently as the thermal bias increases, which can amplify the response in this

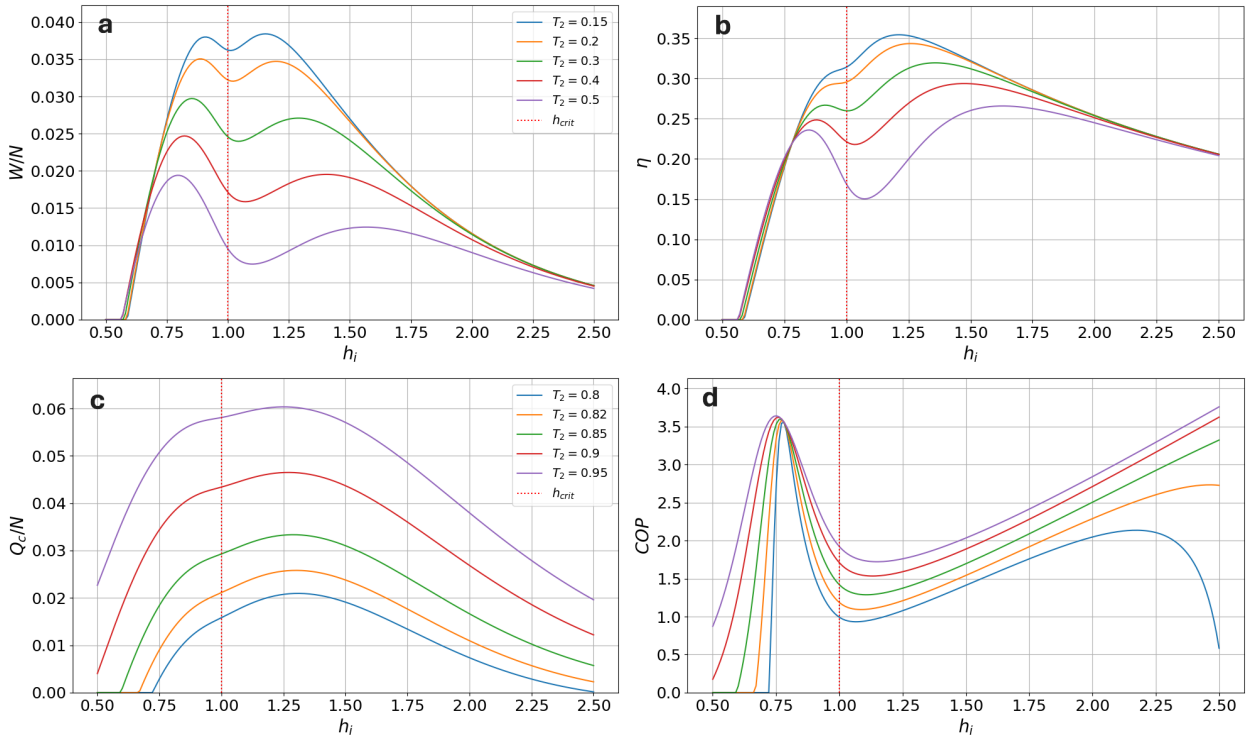

FIG. 4: **(a-b)** Average work per site W/N and thermodynamic efficiency η as functions of the starting transverse field h_i, computed for system size $N = 100$, fixed hot bath temperature $T_h = 1.0$, and different cold bath temperatures ($T_2 \equiv T_c$) ranging over $T_c \in \{0.15, 0.2, 0.3, 0.4, 0.45\}$. The curves reveal two distinct peaks: the first, for $h_i < h_{\rm crit}$, originates from quenches spanning the quantum phase transition, while the second, for $h_i > h_{\rm crit}$, corresponds to evolution entirely within the paramagnetic phase. The critical-crossing peak grows more prominent as T_c rises. **(c-d)** Operation as a quantum refrigerator with $T_h = 1.0$ and selected cold temperatures $T_c \in \{0.8, 0.82, 0.85, 0.9, 0.95\}$. The coefficient of performance (COP) is shown using an analogous analysis to the upper panels. In contrast to the heat exchange patterns, near-degenerate regimes (high T_c) display enhanced refrigeration performance specifically when the protocol crosses the critical point, yielding higher COP values as T_c approaches T_h.

parameter region [86]. Transport studies show that the current (and thus the energy exchange efficiency) carries asymmetric signatures depending on the phase and thermal bias; this explains why, at larger ΔT, the paramagnetic component of the peak can dominate.

Overall, the engine displays a clear athermal signature associated with criticality that strengthens under stronger thermal gradients.

Where in the quantum critical point (QCP): critical quantities (quantum correlations, divergence of the Grüneisen parameter) [87] make the system's response qualitatively different from a simple thermal response, and this effect is amplified when the thermal gradient is large enough to massively excite the critical modes [88].

For the refrigerator (Fig. 4(c)–(d)) we again take $N = 100$ and $T_h = 1.0$, but probe $T_c \in \{0.8, 0.82, 0.85, 0.9, 0.95\}$. Performance deteriorates as T_c approaches T_h.

In near-equilibrium (small ΔT) the stationary heat flux J is given by linear response $J \propto \Delta T$ [89, 90]. Thus when T_c approaches T_h we have a drop in fluxes , where in near-equilibrium ($T_c \to T_h$) the thermal driving force vanishes and the flux follows linear response , hence the concomitant decrease in Q_c/N and COP causes a loss of efficiency .

Near-equilibrium conditions (small ΔT) reduce the refrigerator's ability to pump heat, although a residual enhancement persists close to the critical field owing to the same critical susceptibilities that benefit the engine.

Importantly, unlike the engine, the refrigerator does not exhibit pronounced athermal behavior before versus after the transition; its response is primarily governed by the magnitude of the thermal gradient.

The athermal effects tied to spectral structure are largely masked as soon as ΔT is small the engine measures the system's ability to convert an energy difference into work , this can reveal the spectral structure and increased fluctuations (athermal) [91, 92]. The refrigerator, which aims to move heat against a gradient, depends strongly on the gradient magnitude and transport coefficients; if ΔT is small, the "athermal" component (quantum structure) is subordinate and barely visible. Transport studies [93, 94].

In summary, the critical field $h_i = 1$ plays a central role for both devices by leveraging quantum criticality to boost work and heat exchange, with the effect most evident under large thermal gradients (e.g., high T_h, low T_c for the

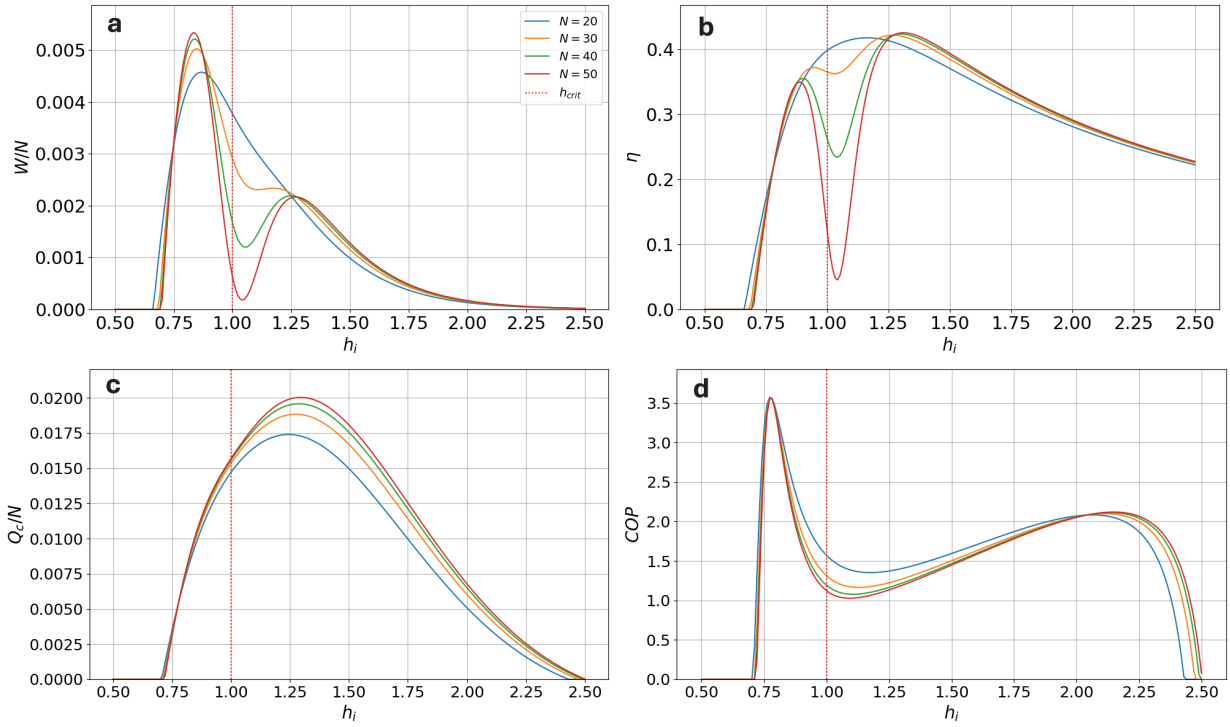

FIG. 5: **(a)** The work per spin, denoted as W/N, is analyzed as a function of the initial transverse field h_i across various system sizes $N \in \{20, 30, 40, 50\}$, with cold reservoir temperatures set at $T_c = 0.16$ and cold reservoir at $T_h = 0.45$. **(b)** The lower panels replicate the analysis of the upper panels but focus on the efficiency of the heat engine, η. The critical field, $h_{\text{crit}} = 1$, is indicated by red dotted lines . **(c)** The upper panels present the heat extracted from the cold reservoir per spin, denoted as Q_c/N, as a function of the initial transverse field h_i, evaluated across various system sizes N, with cold reservoir temperatures of $T_c = 0.8$ and hot reservoir $T_h = 1.0$. **(d)** the analysis mirrors that of the upper panels but focuses on the coefficient of performance (COP) of the refrigerator.

engine; conversely, small ΔT undermines refrigeration performance). These results underscore the interplay between divergent thermodynamic susceptibilities (specific heat and magnetic susceptibility) and nonequilibrium driving in shaping the operation of quantum thermal machines [76–78]. The findings therefore emphasize that optimizing such devices requires careful tuning of reservoir temperatures in conjunction with control of the working-medium parameters to exploit or mitigate critical effects.

C. Spin influence

In this section, we shall examine the influence of correlations between particles and their consequential impact upon the performance of quantum heat engine and refrigerator modes Fig.5, by changing the system size N in fixed cold and hot reservoirs. The performance of a heat engine is defined by two main factors: the work output, W, and the efficiency, η. Our focus here is on determining and analyzing the parameter ranges that optimizes both quantities.

To isolate non-extensive effects we normalize all extensive quantities by N and present the work per spin W/N and the efficiency η as functions of the initial transverse field h_i. Panels (a)–(b) display these observables for a range of system sizes while holding the reservoirs at $T_h = 0.45$ and $T_c = 0.16$. A salient feature is the emergence of a double-peak structure in both W/N and η: a *critical peak* appearing for $h_i < 1$ (associated with quenches that traverse the quantum critical point $h_{\text{crit}} = 1$) and a *paramagnetic peak* located at $h_i > 1$ (corresponding to quenches confined to the paramagnetic phase).

In the paramagnetic phase is to leading order insensitive to N , this can be explained by the correlation length wich is short, so spins are weakly correlated at long distances ,and is small compared to system size $\Rightarrow$ spatial correlations decay rapidly; energy exchanged during strokes is mostly local [95]. contributions are essentially local and additive, so the engine behaves like a collection of single-spin Otto engines

In contrast, the critical peak shows pronounced size dependence: the divergence of correlations at the QCP is limited by finite system size, leading to collective enhancement (finite-size scaling) of W/N and η; characterize how long-range correlations near the QCP enhance the collective response [96]. Explaining why fluctuation-related quantities would diverge in the thermodynamic limit and turn into strongly N-dependent peaks in finite systems. characterize how long-range correlations near the QCP enhance the collective re-

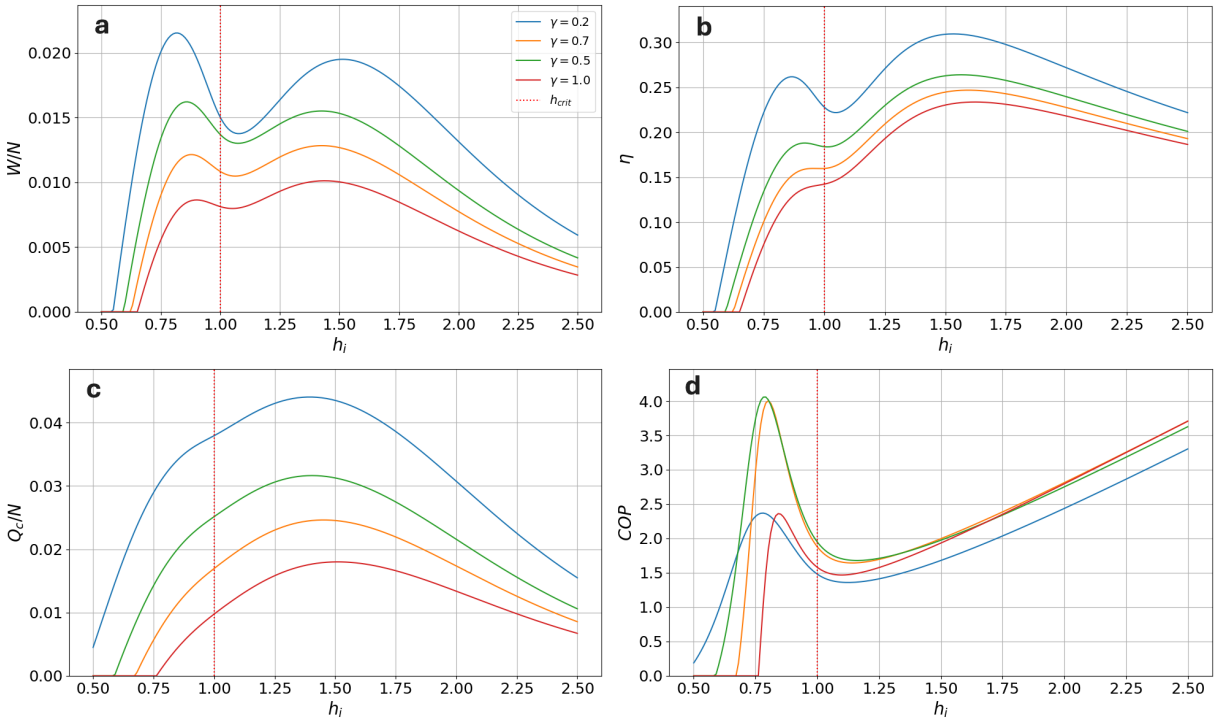

FIG. 6: **(a)** The work per spin, denoted as W/N, is analyzed as a function of the initial transverse field h_i across various system anisotropy γ, with cold reservoir temperatures set at $T_c = 0.16$ and cold reservoir at $T_h = 0.45$ varying $\gamma \in \{0.2, 0.5, 0.7, 1.0\}$. **(c)** The lower panels replicate the analysis of the upper panels but focus on the efficiency of the heat engine, η. The critical field, $h_{\text{crit}} = 1$, is indicated by red dotted lines. **(c)** The upper panels present the heat extracted from the cold reservoir per spin, denoted as Q_c/N, as a function of the initial transverse field h_i, evaluated across various system sizes N, with cold reservoir temperatures of $T_c = 0.9$ and hot reservoir at $T_c = 1.0$. **(d)** the analysis mirrors that of the upper panels but focuses on the coefficient of performance (COP) of the refrigerator.

sponse.

Panels (c)–(d) report the refrigerator performance: the upper panels show the heat extracted per spin Q_c/N versus h_i across several N, and the lower panels show the corresponding coefficient of performance (COP). These results were obtained for $T_h = 1.0$ and $T_c = 0.8$. Consistent with previous studies [10], when the cold-reservoir temperature is relatively large one observes a pre-transition sensitivity to N.

Indicating locally dominated absorption; in contrast, COP as a ratio can amplify residual critical signatures (especially at higher T_c) and reveal a weak subcritical peak , pre-transition N-sensitivity when T_c is relatively large thermal modes are more populated; if the unitary stroke crosses regions with small gap, collective contributions (correlated over sites) [98] manifest before the proper transition, and these depend on network size (larger spatial radius modes).

In the large thermal-gap scenario considered here, however, the dependence on system size is markedly weaker and is followed by a sharp decline across the phase boundary; this size sensitivity is further suppressed at still larger T_c. The extracted heat Q_c/N is generically convex in h_i and shows only a mild N-dependence, whereas the COP can reveal residual signatures of criticality for higher T_c,

And gives asymptotic correlation function forms and show how local observable response varies with h and model parameters: convexity of $Q_c/N(h)$ is expected when per-site absorption is dominated by regular local contributions plus a local critical bump [99], show that COP and other thermodynamic quantities can retain criticality signatures even when Q_c/N is smooth — COP as a ratio (sensitive to relative changes between Q_c and input work) can amplify small structures and make residual critical effects visible. (e.g., if W_{in} drops locally faster than Q_c, COP rises) — hence residual critical signatures detectable in COP while Q_c/N appears smooth.

In particular, a distinct sub-critical peak at $h_i < 1$ persists and scales with N, reinforcing the conclusion that quantum critical fluctuations can enhance collective refrigeration effects under appropriate thermal conditions.

The strokes involves QCP crossing, long correlation length and mode coupling allow collective responses: extracted energy (or pumped heat) becomes coherent over multiple sites and evolves non-trivially with N. Observed subcritical peak scaling in your data is the expected signature of collective enhancement via critical fluctuations [101]; , effectively enhance refrigeration under suitable thermal conditions .

In summary, finite-size correlations selectively amplify thermodynamic response near the quantum critical point: the engine's critical peak is strongly size-dependent and reflects cooperative phenomena, while the paramagnetic response re-

mains essentially extensive. For the refrigerator, size effects are more subtle and contingent on the thermal gap; close to equilibrium (small ΔT) the device shows little finite-size sensitivity, whereas larger gaps can reveal N-dependent critical features. These findings highlight the dual role of reservoir temperatures and quantum criticality in sculpting the operational landscape of many-body quantum thermal machines, and they point to system size as a practical knob for enhancing or suppressing collective performance.

D. The impact of anisotropy

This section analyzes the influence of anisotropy on the thermodynamic performance of the quantum Otto machine, with emphasis on features induced by the quantum phase transition (see Fig. 6). Panels (a)–(b) summarize the heat-engine behaviour:

For low anisotropies γ the system extracts on average more energy per site and achieves higher efficiencies near the critical regime [101] : effective gap reduction and increased low-energy mode density , make modes thermally accessible and favor collective exchanges.

Increasing γ brings the system closer to transverse Ising ($\gamma \to 1$) where spectrum and excitation nature change (typically larger gap depending on diagram point). Gap opening (or reorganization) makes energy response less sensitive to small h variations with transition effect becomes smoother (less abrupt) [103]. Additionally, suppression of available low-energy modes reduces W/N.Concurrently the paramagnetic peak (located at $h_i > 1$) gains prominence, particularly around $\gamma = 1$. Thus, low γ favors enhanced critical responses, whereas larger anisotropy shifts the balance toward paramagnetic operation and smooths the transition-induced features.

For high γ (near Ising), paramagnetic-side dynamics and spectrum favor excitations that, though more local, can be efficiently exploited by the cycle depending on h_i trajectory. Result is a sharper, sometimes dominant paramagnetic peak as local contributions become more coherent and additive (hence robust peak at $h > 1$). We observes this reversal between critical and paramagnetic contributions depending on parameters.γ modulates dominant excitation nature (collective low-energy vs local) [102]. Low γ favorizes more gapless modes with amplified critical responses. High γ have a more local behavior with larger gap, additive paramagnetic peaks, softened features.

The efficiency η mirrors these trends: it attains its highest values for small γ, with a pronounced suppression at the critical field $h_{\rm crit} = 1$.

Efficiency η (η_R) depends on work(absorbed heat ratio). For small γ, greater extractable energy per spin (accessible critical modes) often translates to better conversion if losses are controlled to high η. However, sharp suppression at $h = 1$ may come from non-adiabatic irregularities or abrupt gap change (more dissipation) [104], leading to η dip exactly at QCP if protocol is not ideally slow.

Panels (c)–(d) report the refrigerator metrics.

We observe that Q_c/N increases for low anisotropies γ, especially in the paramagnetic sector: reducing γ brings the model closer to the XX case, increases the density of thermally accessible modes and allows greater heat absorption per site [105] .

COP = $|Q_c|/W_{\rm in}$ depends on both absorbed energy and input work. As γ increases from 0, two effects compete: (a) partial gap opening reduces irreversible losses (improving COP); (b) excitation structure change makes conversion less favorable (relative Q_c reduction or $W_{\rm in}$ increase)[106, 107]. The trade-off can produce an intermediate optimum ($\gamma \approx 0.7$ per your numerical parameters). Beyond a certain anisotropy threshold (post-critical), spectrum reorganization suppresses critical advantage and COP drops then stabilizes. The anisotropy enhance efficiency in certain ranges and the effect is strongly parameter-dependent , and convertible heat fraction .

In summary, anisotropy controls the switch between collective mechanisms (low γ, enhanced extraction) and gapped-spectrum behaviors (high γ, COP potentially improved up to a threshold) [108, 109].

In short, whereas small anisotropy amplifies heat extraction and critical enhancement, larger anisotropy can improve refrigeration performance up to a threshold beyond which critical advantages are lost.

These observations can be rationalized in terms of many-body quantum correlations. Small γ preserves stronger quantum coherence and nonlocal correlations (entanglement and spin–spin correlations) [79, 80], which amplify collective responses near criticality and thus boost engine performance. Large anisotropy suppresses critical fluctuations and drives the system toward a more classical paramagnetic-like regime: this stabilizes dynamics but reduces the capacity to harness critical energy fluctuations, explaining the observed saturation and subsequent fall-off of the COP at high γ. The saturation phenomenon may therefore indicate a practical quantum bound: when correlations are overly quenched, the advantages conferred by the phase transition can no longer be exploited, producing a sharp degradation in thermodynamic performance.

Overall, the anisotropy parameter γ emerges as a key control knob for tailoring operational regimes of quantum thermal machines: tuning γ allows one to trade off between exploiting critical, cooperative enhancements and attaining robustness associated with paramagnetic-like behaviour.

E. Influence of the symmetric off-diagonal interaction

We now examine the impact of the The symmetric off-diagonal interaction Γ , on the thermodynamic performance of the quantum Otto machine, focusing on behavior near the quantum phase transition (see Fig. 7). The Γ coupling introduces an symmetric, chiral term $\propto \vec{D} \cdot (\vec{S}_i \times \vec{S}_j)$ that competes with conventional exchange interactions and thereby alters both the spectral structure and collective dynamics of the spin chain [62, 82].

For the heat engine (Fig. 7a–b), the work per spin W/N attains its largest values immediately before the transition when

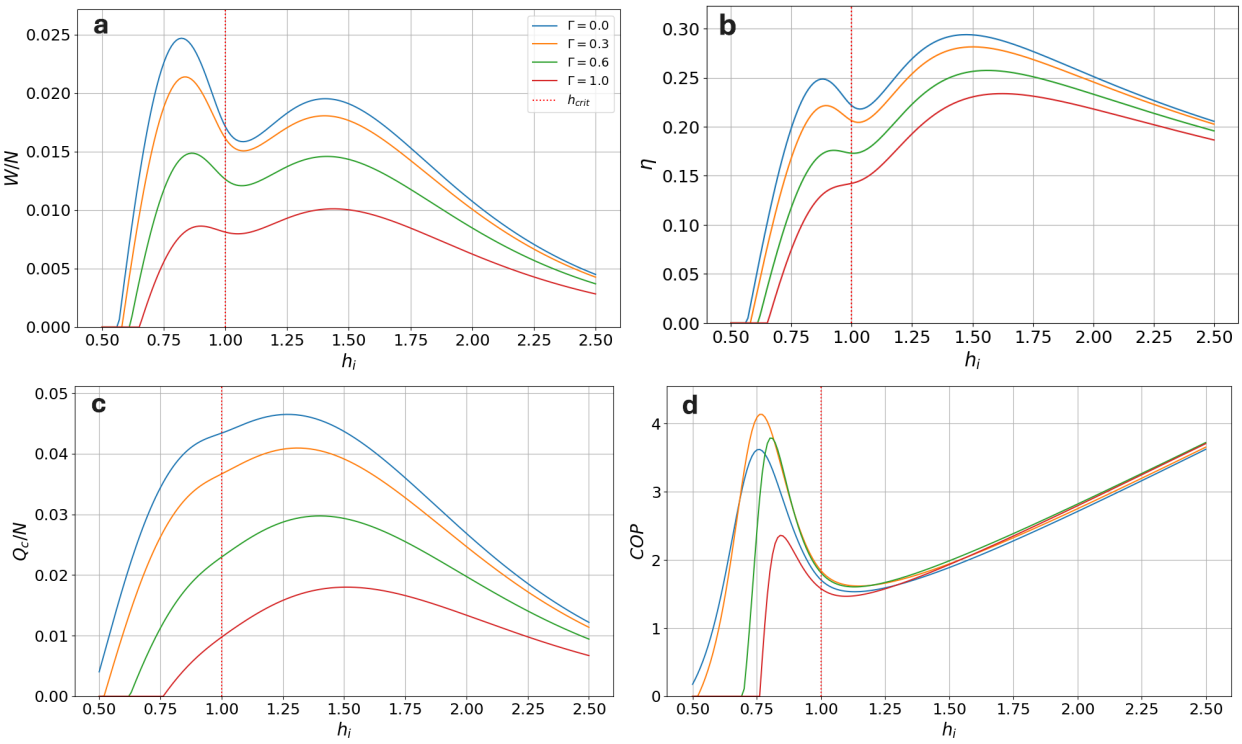

FIG. 7: **(a)** The work per spin, denoted as W/N, is analyzed as a function of the initial transverse field h_i across various γ interaction intensity Γ with cold reservoir temperatures set at $T_c = 0.16$ and cold reservoir at $T_h = 0.45$ varying $\Gamma \in \{0.0, 0.3, 0.6, 1.0\}$. **(b)** The lower panels replicate the analysis of the upper panels but focus on the efficiency of the heat engine, η. The critical field, $h_{\text{crit}} = 1$, is indicated by red dotted lines **(c)** .The upper panels present the heat extracted from the cold reservoir per spin, denoted as Q_c/N, as a function of the initial transverse field h_i, evaluated across various system sizes N, with cold reservoir temperatures of $T_c = 0.9$ and hot reservoir at $T_c = 1.0$. **(d)** the analysis mirrors that of the upper panels but focuses on the coefficient of performance (COP) of the refrigerator.

Γ is small, with the global maximum located at $\Gamma = 0$.

The chain retains the "standard" alignment dictated by the exchange and the transverse field. The collective excitations (low-energy modes near the QCP) are coherent and extended across the lattice $\rightarrow$ they can be coordinated by the strokes of the Otto cycle to store and then release energy efficiently. * The work extracted per unitary stroke results from the reorganization of the level occupations. If the spectrum features many weakly energetic modes (small gap) [110], a small parameter variation (field) allows significant energy displacement between levels — hence a large W. Without The symmetric off-diagonal interaction, the level structure favors this collective transfer, hence the maximum at $\Gamma = 0$.

This indicates that weak or vanishing Γ coupling preserves spin alignment and coherent collective response, which favor efficient energy extraction in the pre-critical regime. As Γ increases, the Γ term introduces magnetic frustration and spin misalignment; consequently W/N decreases and the dominant extraction feature shifts into the paramagnetic sector.

The Γ term is symmetric and favors canting chiral order rather than simple ferromagnetic alignment. It breaks local alignment and tends to decorrelate spins from each other: coherent collective modes are weakened. Frustration and canting result in: (i) modification of the spectrum (reordering of levels, opening/closing of gaps at different k points), (ii) reduction of the effective correlation length of the participating modes, (iii) partial localization of excitations. These effects reduce the efficiency of collective energy transfer to W/N decreases. In the strongly gapped paramagnetic regime, the contributions become local and additive (each site or small subregion provides an independent contribution). When collective modes are suppressed by off-diagonal interaction, the most efficient extraction can occur for field values where the local (paramagnetic) response is favorable — hence the shift of the peak.

In this large-Γ regime, the paramagnetic peak can outperform the critical peak, so that post-critical operation becomes comparatively more effective.

In the strongly gapped paramagnetic regime, the contributions become local and additive (each site or small subregion provides an independent contribution). When collective modes are suppressed by off-diagonal interaction [111], the most efficient extraction can occur for field values where the local (paramagnetic) response is favorable — hence the shift of the peak.

The efficiency η displays a complementary but nontrivial pattern: the paramagnetic phase generally yields higher η, especially for small Γ, whereas near the critical field the ef-

ficiency either falls sharply (for weak γ coupling) or varies smoothly (for stronger Γ), reflecting the interplay between enhanced susceptibility, instability and the γ-induced modification of level spacings.

The efficiency $\eta = W/Q_h$ (or variant according to your definition). It depends on both the extracted work and the input heat. Two important effects:

If W decreases but Q_h decreases even more, η can increase. In the local paramagnetic regime, the heat input per site can be lower (fewer excitations to sustain) . Near the QCP, the very strong susceptibility (large χ_F, large C) can amplify the Q_h required to produce a small energy gain or generate dissipation via non-adiabatic excitations; if the protocol is not slow enough, these irreversibilities cause η to drop.

The influence of the The symmetric off-diagonal interaction modifies the energy level spacings and the density of states. If Γ smooths the variation of levels around the QCP (spectral reordering), the response in h becomes gentler, the drop in η at the QCP is damped . If Γ is weak, gap closure and high sensitivity make the exchange more fragile (non-adiabatic excitations) with abrupt drop in η [112]. In summary: Γ acts as a spectral damper: it can reduce the amplitude of fluctuations (and losses related to non-adiabaticity), making $\eta(h)$ smoother. Adiabaticity finite-time: if unitary strokes are too fast, non-adiabatic excitations are created, increasing losses. The effect is maximal near the QCP (small gap) and accentuates the drop in η if Γ is weak. Coupling to reservoirs (local vs global, Markovianity): the way baths inject/extract heat controls whether exchanges exploit local or global modes. Certain coupling structures restore collective efficiency even when Γ is moderate. Finite size N: the critical peak scales as predicted by finite-size scaling (amplitude/width); the role of off-diagonal interaction can modify effective exponents or simply the constant in the scaling. Testing several N is essential. Temperature thermal gradient: the visibility of collective effects depends on the thermal occupation of modes: if T is too high, modes can saturate; if too low, access to low-energy modes is reduced.

For the refrigerator (Fig. 7c–d), the extracted heat per spin Q_c/N follows an analogous trend: maximal cooling is observed at small Γ, where coherent collective modes and large susceptibilities facilitate effective heat uptake.

Collective modes susceptibility: near the critical point (or in the pre-critical regime), the chain has numerous low-energy excitations that are strongly correlated (long correlation length ξ, high density of low-ε modes). These modes allow efficient reception and storage of energy when an isochore connects the system to the cold reservoir: a small variation in mode population yields a large local energy variation with large Q_c. Why small Γ helps: the off-diagonal interaction (symmetric term) tends to break alignment and confine the fragment modes [113]. For $\Gamma \approx 0$, these modes remain extended and coherent; the susceptibility (e.g., fidelity susceptibility χ_F, derivatives of correlations) is large and enables efficient heat pumping per site. Where that informational quantities (QFS, WYSI) and correlation derivatives exhibit singularities(log-divergences) at the QCP and grow with N [114] , these are precisely the signatures that enable high Q_c/N when coupling the system to the cold reservoir.

The coefficient of performance (COP) behaves nonmonotonically with Γ: it increases with Γ up to an intermediate optimum (empirically near $\Gamma \approx 0.5$), after which further strengthening of the off-diagonal interactionsuppresses coherence and reduces COP.

And it depends on both the pumped heat and the input work. Two competing effects as Γ increases: Damping of losses: a slight increase in Γ can modify certain gaps and reduce non-adiabatic transitions or parasitic couplings to baths wich decrease in irreversible losses to COP rises. Destruction of coherence: beyond a threshold, Γ fragments collective modes, reduces useful low-ε density, and increases dissipation. Intermediate optimal value: the non-monotonic behavior (optimum ≈ 0.5 here) corresponds to the balance point between these two effects: enough symmetric off-diagonal interaction to reduce certain losses, but not too much to break collective coherence.

Beyond the transition the COP partially recovers and becomes relatively insensitive to Γ in the strongly paramagnetic regime, consistent with a crossover to more diffusive, incoherent heat transport.

The strongly gapped paramagnetic phase or when dominated by local fluctuations, thermal exchanges become mainly local and incoherent. The role of extended modes is weak; absorption and transport occurs via local transitions that depend little on the fine details of the Γ coupling. Non-equilibrium transport studies show that for strong Γ , thermal conduction shifts from more coherent regimes to more diffusive regimes — this change explains the weakening of the COP-Γ dependence. For h strongly paramagnetic, plot COP vs Γ for several N: curves overlap to a weak dependence. Transport behavior measurement: stationary current J vs Γ shows plateau with low sensitivity in paramagnetic regime.

Physically, these findings reflect a balance between two competing effects of the symmetric off-diagonal interaction . At small Γ, the symmetric off-diagonal interaction term opens additional transition channels and enhances the system's responsiveness to driving, thereby improving thermodynamic performance. At large Γ, however, the induced frustration and loss of spin alignment undermine quantum coherence, perturb the level structure and impede collective dynamics—effects that collectively reduce work extraction and refrigeration efficiency. The observed intermediate optimum (e.g. COP peaking around $\Gamma = 0.5$) highlights that moderate chiral coupling can be beneficial, while excessive Γ strength is detrimental.

In summary, Γ constitutes an effective control parameter for tuning quantum thermodynamic cycles: judicious adjustment of the Γ interaction can enhance either engine or refrigerator operation, but over-driving the chiral coupling quenches the cooperative phenomena that underpin superior performance. These results thus underscore the subtle interplay between chirality, critical fluctuations and nonequilibrium thermodynamics in many-body quantum heat engines. [62, 82]

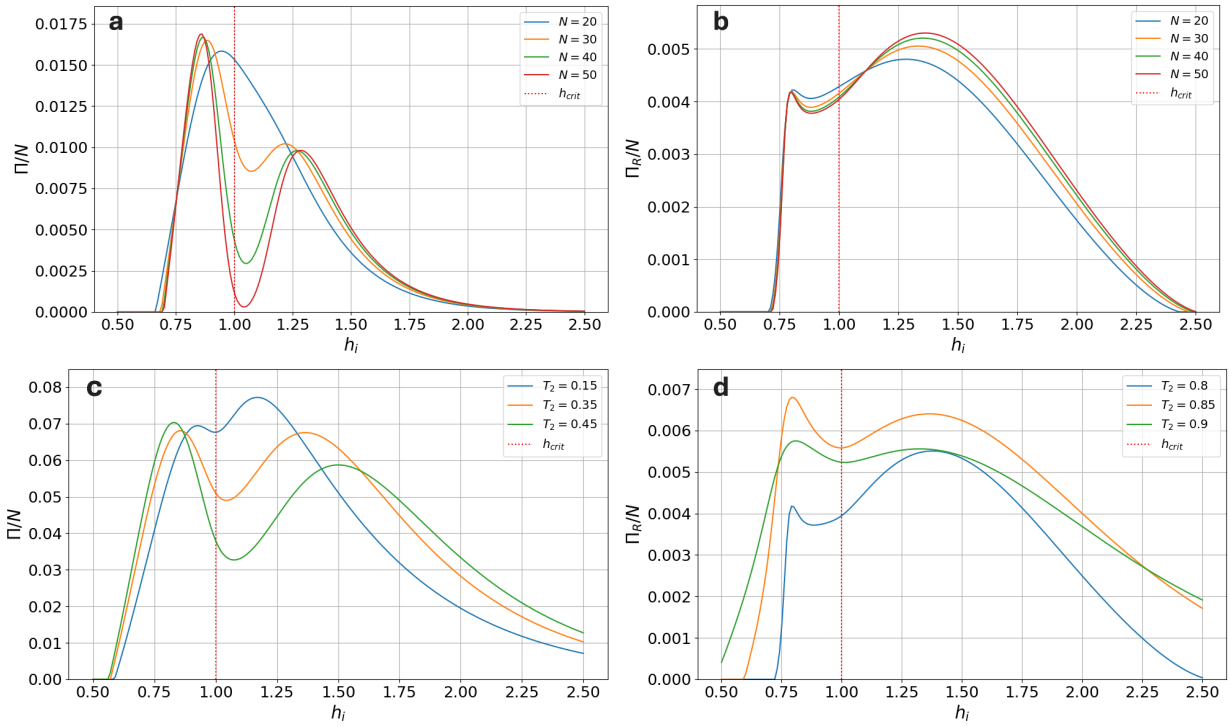

FIG. 8: **(a)** The Scaling Factor per spin, denoted as Π/N, is analyzed as a function of the initial transverse field h_i across various system size , with cold reservoir temperatures (for our case $T_2 \equiv T_c$) set at $T_c = 0.16$ and hot reservoir at $T_h = 0.45$ varying $N \in \{20, 30, 40, 50\}$.**(b)** The lower panels replicate the analysis of the upper panels but focus on the Scaling Factor per spin Π_R/N of quantum refrigerator. The critical field, $h_{\text{crit}} = 1$, is indicated by red dotted lines. **(c)** The upper panels present Π/N as a fonction of h_i, evaluated at various temperature of the cold reservoir $T_c \in \{0.15, 0.35, 0.45\}$, with fixed hot reservoir temperature $T_h = 1.0$. **(d)** The analysis mirrors that of the upper panels but focuses on Π_R/N of the quantum refrigerator with varied $T_c \in \{0.8, 0.85, 0.9\}$ and fixed T_h=1.0.

IV. SCALING FACTOR

A. Critical effect on the stabilty of the system

The factor Π serves as a metric to assess how proficiently a heat engine extracts mechanical output, notwithstanding an efficiency that remains below the theoretical Carnot maximum [81]

$$\Pi = \frac{W}{\eta_{\text{Carnot}} - \eta}. \tag{18}$$

A high scaling factor means that the system is optimized to extract significant work, even in non-ideal conditions. In quantum engines, a higher Π reflects more efficient energy conversion through quantum effects like correlations and superposition. It also suggests lower energy losses, allowing the system to approach Carnot efficiency. Overall, a high scaling factor indicates that the system is productive, efficient, and resilient to fluctuations.

It is not evident whether the absolute maximum of Π corresponds to the critical point or to the paramagnetic peak. Since critical behavior becomes more pronounced with increasing system size, relatively large values of N might be required in order to capture the effects of critical enhancement. It is worth noting that, while the height of the paramagnetic peak in Π/N displays a conventional linear scaling, $\Pi \sim N$, the critical peak exhibits a growth that appears to be faster than linear.

We now proceed to investigate the influence of the the stability of the operational regimes across different system sizes Fig.8-a, particular attention is devoted to how variations in the temperature T_c Fig.8-c affect the location and nature of the performance maxima.

A substantial enhancement in engine performance is illustrated in Fig.8-a, where the thermodynamic efficiency metric per spin Π/N is plotted as a function of the initial transverse field h_i. In the presence of a pronounced temperature gradient between the reservoirs, optimal performance is generally achieved when quenches are carried out within the paramagnetic phase. Conversely, increasing the temperature of the cold reservoir reduces the overall temperature gradient, thereby limiting heat absorption and suppressing work production away from criticality. Under such conditions, the performance peaks of Π tend to align with the critical field $h_i = h_{\text{crit}}$, indicating that energy conversion becomes less efficient far from criticality but is enhanced near the critical point. Nevertheless, predicting whether the global maximum of Π occurs at the critical or paramagnetic peak remains non-

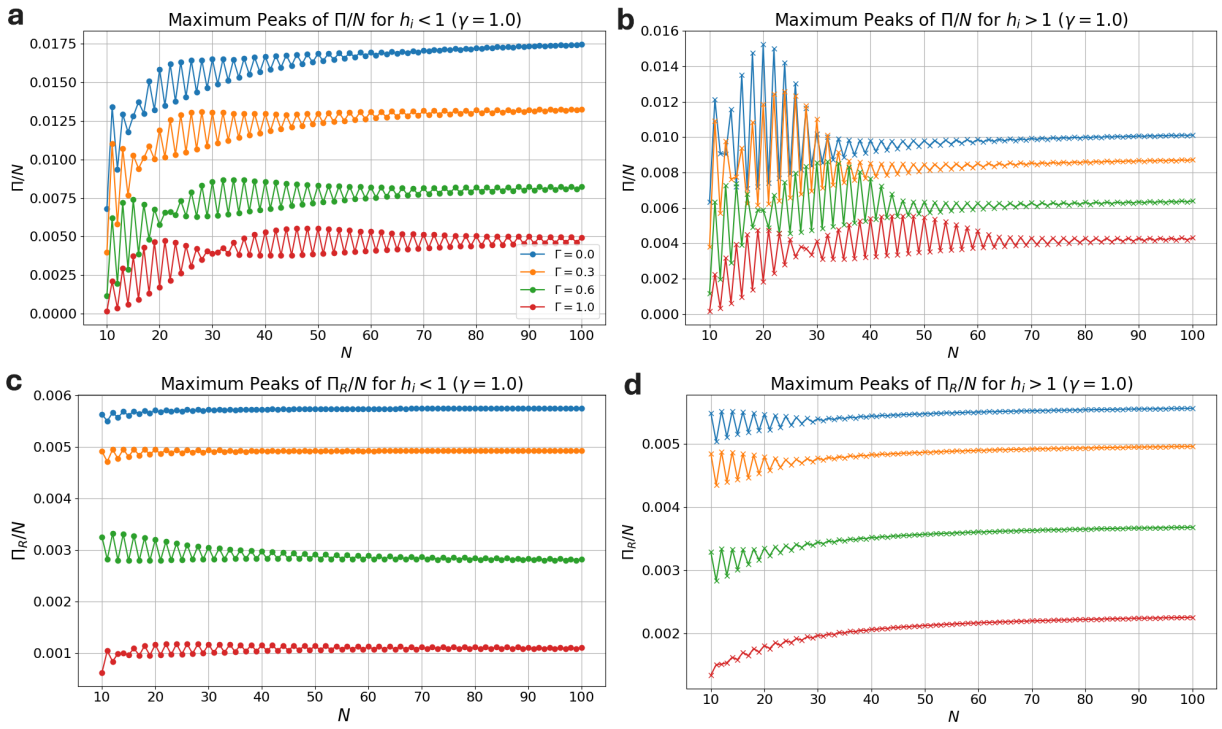

FIG. 9: **(a-b)** Behavior of the maxima of the critical and of the paramagnetic peak of Π/N versus N for the engine mode (E), with $T_c = 0.16$ and $T_h = 0.45$ varying $\Gamma \in \{0, 0.3, 0.6, 1.0\}$. **(c-d)** Bottom panels: behavior of the maxima of the critical and of the paramagnetic peak of Π_R/N versus N, varying $\Gamma \in \{0, 0.3, 0.6, 1.0\}$ for $T_c = 0.9$ and $T_h = 1.0$ for the refrigerator mode (R).

trivial. Furthermore, since critical phenomena become more pronounced with increasing system size, relatively large values of N may be required to fully harness critical enhancement effects.

In analogy with the engine mode (E), we define a complementary quantity to assess the refrigerator performance:

$$\Pi_R = \frac{Q_c}{\delta\eta_R}, \tag{19}$$

where $\delta\eta_R = \eta_C^R - \eta^R$ denotes the deviation of the refrigerator's coefficient of performance (COP) from the Carnot limit. Fig.8-b presents the behavior of Π_R/N for the same parameter set as our previous results.The plots 8-d shows that the optimal refrigeration performance is consistently achieved within the paramagnetic phase, regardless of system size. The augmentation of the critical peak becomes distinctly apparent when examining the performance trends as a function of the transverse field for differente thermal gaps similar to that reported for the study of the Ising [10] and long-range Ising models [74]. However, in our case, a larger thermal gap was chosen, which preserves the refrigerator (R) operational mode without switching to the quantum heat engine (E) regime. As a result, the dependence of the critical peak on the chain size is weaker compared to [10]. Unlike the engine (E) mode , we observe that the stability and performance do not depend significantly on the thermal gap ΔT in the the (R) mode for a fixed N. Specifically, Π_R/N is larger for intermediate temperatures compared to cases where ΔT is either narrower or broader. In particular, for small systems, the discretization of energy levels, boundary effects, and the absence of a true thermodynamic limit significantly influence the energy exchange processes. These effects can lead to fluctuations and non-extensive behaviors in quantities such as heat and work per spin. For example, the specific heat of finite spin chains shows strong fluctuations and non-monotonic behavior for small N, before stabilizing into an intensive quantity as N increases [117, 118]. Additionally, quantum coherence and entanglement, which play a significant role in small quantum systems, can enhance or suppress the performance of quantum thermal machines. These effects are negligible in the thermodynamic limit but can substantially affect observables such as work and efficiency at small N[119, 120]. This highlights the emergence of distinctly non-classical thermodynamic signatures in small quantum systems [121, 122]. Moreover, boundary contributions in finite spin chains are non-negligible when N is small, altering local and global observables, including the effective energy exchange per spin [123, 124]. Therefore, the tendency of the work/heat per spin to become independent of N in the large-N limit aligns well with the extensivity principle of thermodynamics. For small N, however, the observed behavior is fully consistent with the known physics of finite-size quantum systems[125, 127].

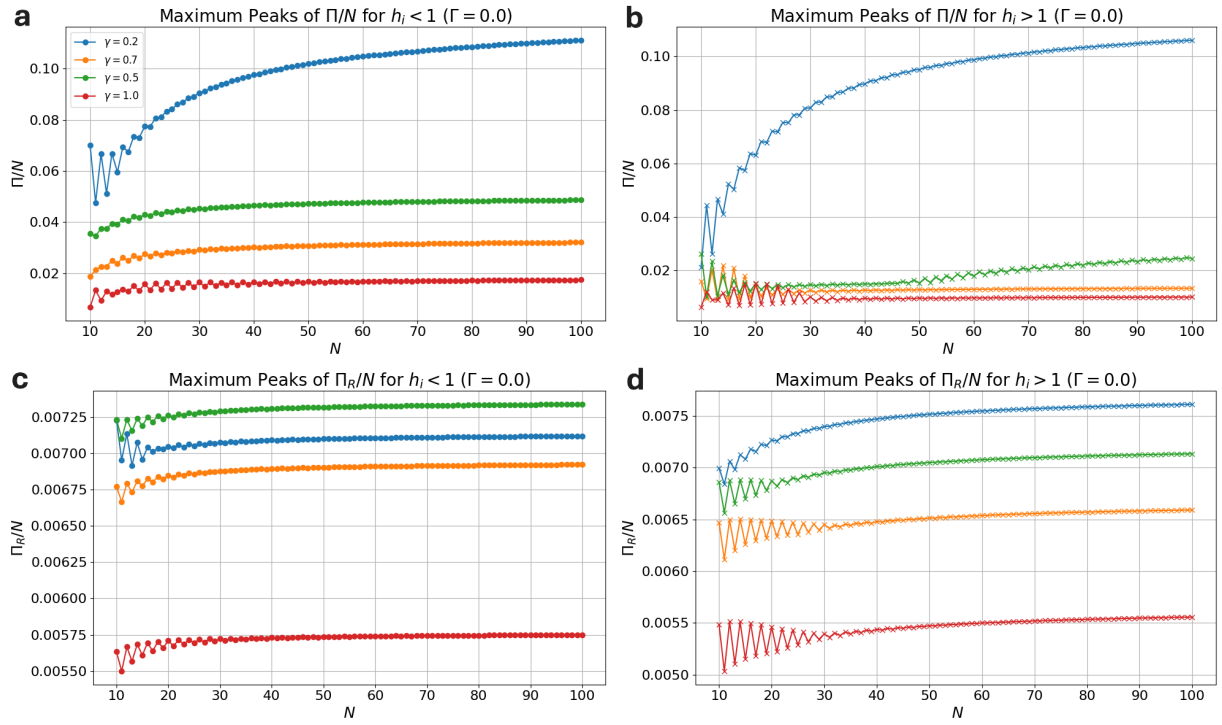

FIG. 10: **(a-b)** Evolution of the maximum values of Π/N as a function of chain length N in the heat-engine regime (E), at temperatures $T_c = 0.16$ and $T_h = 0.45$, for several anisotropy strengths $\gamma \in \{0.2, 0.5, 0.7, 1.0\}$. Distinct curves illustrate the height of the critical peak and that of the paramagnetic peak. **(c-d)** Lower panels: size dependence of the peak amplitudes of Π_R/N in the refrigerator regime (R), with $T_c = 0.9$ and $T_h = 1.0$, and the same set of γ values $\gamma \in \{0.2, 0.5, 0.7, 1.0\}$. The data separate the contributions from the critical and paramagnetic maxima.

B. Enhancement of the performance with the system size

The enhancement of the critical peak becomes evident when the performance is examined as a function of system size. To quantify this effect we perform regression fits to extract a scaling exponent a such that the relevant peak amplitude (per spin) scales as N^a. This analysis distinguishes three regimes—small, intermediate and large chains—and permits a direct comparison between peaks located in the paramagnetic sector (pre-transition) and those appearing in the ferromagnetic sector (post-transition).

For the quantum heat engine (Fig. 9a–b) increasing the Dzyaloshinskii–Moriya parameter Γ generally reduces performance, an effect that is most pronounced for small N. The fitted exponent grows from $a = 0$ at $\Gamma = 0$ to $a \approx 0.23$ at $\Gamma = 1$, indicating that finite-size fluctuations migrate toward intermediate chain lengths and produce an enhanced (nearly linear) N-dependence for the engine mode. In physical terms, larger Γ accelerates the crossover from vanishing-size scaling to a regime with appreciable system-size sensitivity.

By contrast, the refrigerator (Fig. 9c–d) displays a distinct response. While stronger Γ reduces absolute stability, it simultaneously weakens the size dependence: the exponent controlling the paramagnetic peak decreases from $a \approx 0.0055$ at $\Gamma = 0$ to $a \approx 0.001$ at $\Gamma = 1$. Thus, although increasing the off-diagonal coupling lowers overall performance, it also suppresses the growth rate with N, yielding qualitatively similar behavior on both sides of the transition.

Anisotropy produces related but distinguishable effects. For the engine mode (Fig. 10a–b) the exponent drops from $a \approx 0.34$ at $\gamma = 0.2$ to $a \approx 0$ at $\gamma = 1$. This trend indicates that small γ amplifies sensitivity to N (approaching near-linear scaling in the critical regime), whereas large γ drives the system toward classical, extensive or saturated behaviour ($\Pi/N \sim 1$). The qualitative response is similar before and after the phase transition, but post-critical dynamics become more classical and less dependent on system size as γ increases.

For the refrigerator (Fig. 10c–d), intermediate anisotropy ($\gamma \approx 0.5$) confers slightly better stability than very low anisotropy: the fitted exponents are $a \approx 0.0072$ at $\gamma = 0.5$ versus $a \approx 0.0070$ at $\gamma = 0.2$, both indicating a very weak N-dependence. After the transition a more linear, size-sensitive behaviour emerges, mirroring the tendencies observed for the engine.

Deviations observed for small N are consistent with finite-size effects: spectral discreteness and amplified fluctuations produce departures from thermodynamic-limit scaling. As N increases these mesoscopic anomalies subside and the system crosses over to the asymptotic scaling captured by the exponent a.

Finally, the enhancement of the critical peak should be viewed as a crossover phenomenon associated with the clos-

ing of the spectral gap Δ at criticality.

V. CONCLUSION

We have introduced a quantum Otto cycle that utilizes a many-body working medium, specifically a transverse-field quantum Ising chain. This system undergoes alternating processes, an unitary evolution driven by a time-varying transverse field [130] and thermalisation while coupled to a thermal reservoir. The dynamics during the thermalisation phases are governed by a nonlocal Lindblad master equation, which provides an accurate representation of the system's interaction with thermal baths [131]. Our analysis of the engine's operational regimes demonstrates that it can function as either a heat engine or a refrigerator across a wide range of parameters, depending on the temperatures of the reservoirs and the characteristics of the thermodynamically adiabatic transformations [132] . To assess the heat engine's performance, we evaluated critical metrics, including the work output, efficiency, and their ratio. These measures reveal a dual-peak pattern: one peak corresponds to quenches spanning the quantum critical point, while the other emerges from quenches within the paramagnetic phase. The peak linked to the quantum critical point becomes more distinct as the temperature difference between the reservoirs decreases, exhibiting a superlinear scaling with system size, which highlights the role of quantum criticality.We further extended our investigation to the refrigerator mode, analyzing the heat extracted from the cold reservoir, the coefficient of performance (COP), and their ratio. Although less prominent than in the heat engine, signatures of quantum criticality remain evident in this configuration. Additionally, we explored the effects of partial thermalisation, shedding light on the behavior of more realistic quantum many-body engines interacting with external baths.

These findings offer valuable insights for near-term experimental implementations using ion traps, which can simulate interacting spin chains with on the order of 10^2 spins. While the engine's absolute performance is typically maximized for quenches within the paramagnetic phase, its scaling with system size N can be optimized for quenches across the critical point. However, the superextensive scaling of the critical peak levels off at large N, suggesting a finite range of system sizes where the performance enhancement near criticality can be effectively harnessed. The figure illustrates an enhanced thermal sensitivity within the paramagnetic phase, which exhibits greater stability and a more pronounced dependence on the thermal gap. In particular, the quantum heat engine demonstrates improved stability for larger thermal gaps ΔT, whereas the refrigerator regime displays the opposite trend. Moreover, both regimes show a tendency toward saturation and reduced fluctuations compared to the behavior observed near the critical point.In this study, we primarily concentrated on the engine's performance in terms of work output (or heat exchanged) per spin. Nevertheless, several areas merit further exploration, including the optimization of power output—a complex challenge requiring detailed consideration of both the thermalisation protocol and the adiabatic transformations . For instance, determining the optimal operating speed would necessitate accounting for the thermalisation timescale [132], which depends on the microscopic properties of the modeled bath. Moreover, it remains uncertain whether a partially thermalised stroke would underperform compared to a fully thermalised one. To address the potential reduction in power output [133] , due to slower parameter adjustments during the adiabatic stroke, advanced methods such as shortcuts to adiabaticity, variational optimization, and reinforcement could be employed [134].Furthermore, examining the statistical distribution of the work output could provide additional experimental insights. The work output may exhibit significant fluctuations, potentially compromising the engine's stability. While these fluctuations are expected to diminish with increasing system size, they may be amplified by quantum criticality. Lastly, the approach outlined here can be readily adapted to systems beyond the bosonic quadratic model used in this work, potentially revealing alternative performance characteristics[135–139].

ACKNOWLEDGMENTS

A.H. acknowledges the financial support of the National Center for Scientific and Technical Research (CNRST) through the "PhD-Associate Scholarship-PASS" program.

Appendix A: Energy Spectrum and Finite-Size Effects

Its Hamiltonian is given by:

$$H = H_{XY} + H_{\Gamma}, \tag{A1}$$

where

$$H_{XY} = J\sum_{n=1}^{L}\Big[\Big(1+\frac{\delta}{2}\Big)\sigma_n^x\sigma_{n+1}^x+\Big(1-\frac{\delta}{2}\Big)\sigma_n^y\sigma_{n+1}^y\Big]+h\sum_{n=1}^{L}\sigma_n^z, \tag{A2}$$

and

$$H_{\Gamma} = \Gamma\sum_{n=1}^{L}\Big(\sigma_n^x\sigma_{n+1}^y + \gamma\,\sigma_n^y\sigma_{n+1}^x\Big). \tag{A3}$$

Here, the operators σ_n^{α} (with $\alpha = x, y, z$) act on the nth site of the chain. The parameters J, δ, and h represent the ferromagnetic coupling, the anisotropy parameter, and the strength of the uniform transverse field, respectively. Additionally, Γ determines the amplitude of off-diagonal exchange interactions, while γ controls their relative weight. We impose periodic boundary conditions ($\sigma_{L+1} = \sigma_1$), with L denoting the length of the spin chain.The analytical solution of this Hamiltonian follows three steps: a Jordan–Wigner transformation, followed by a Fourier transformation, and finally a Bogoliubov transformation. These steps lead to the diagonalized

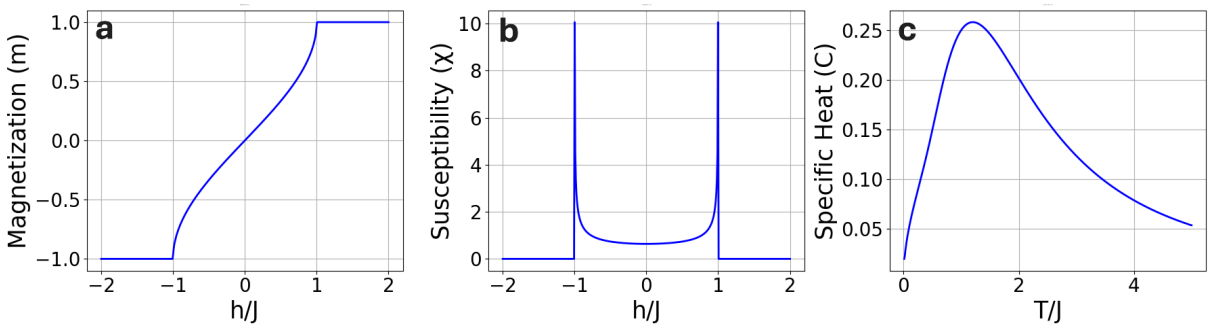

FIG. 11: **(a-b)** The magnetization and the susceptibility of the XX model in the ground-state as a function of h/J. **(c)** Specific heat as a function of the Temperature T/J.

Hamiltonian: The energy spectrum of the system can be efficiently analyzed by employing the Jordan-Wigner transformation [140], which maps spin operators to spinless fermionic operators via the nonlocal relations:

$$\sigma_j^x = -\prod_{l<j}(1-2c_l^\dagger c_l)(c_j + c_j^\dagger), \tag{A4}$$

$$\sigma_j^z = 1 - 2c_j^\dagger c_j, \quad \sigma_j^y = i\sigma_j^x\sigma_j^z, \tag{A5}$$

where c_j ($c_j^\dagger$) annihilates (creates) a spinless fermion at site j and the canonical anticommutation relations $\{c_i, c_j\} = \{c_i^\dagger, c_j^\dagger\} = 0, \{c_i^\dagger, c_j\} = \delta_{ij}$.

Applying the Jordan–Wigner transformation to the Hamiltonian , yields a quadratic fermionic form which naturally separates into bulk and boundary contributions,

$$\hat{H} = \hat{H}_b + \hat{H}_e. \tag{A6}$$

The bulk part reads

$$\begin{aligned}\hat{H}_b = \sum_{j=1}^{N-1} \Big[&(-c_j c_{j+1}^\dagger - \gamma c_j c_{j+1} + \gamma c_j^\dagger c_{j+1}^\dagger + c_j^\dagger c_{j+1}) \\ &+ i\Gamma(-c_j c_{j+1}^\dagger + c_j c_{j+1} + c_j^\dagger c_{j+1}^\dagger - c_j^\dagger c_{j+1}) \\ &+ i\Gamma\alpha(c_j c_{j+1}^\dagger + c_j c_{j+1} + c_j^\dagger c_{j+1}^\dagger + c_j^\dagger c_{j+1})\Big] \\ &+ h\sum_{j=1}^{N}(1-2c_j^\dagger c_j).\end{aligned} \tag{A7}$$

The edge term arising from the Jordan–Wigner string is

$$\begin{aligned}\hat{H}_e = s\Big[&(-c_N c_1^\dagger - \gamma c_N c_1 + \gamma c_N^\dagger c_1^\dagger + c_N^\dagger c_1) \\ &+ i\Gamma(-c_N c_1^\dagger + c_N c_1 + c_N^\dagger c_1^\dagger - c_N^\dagger c_1) \\ &+ i\Gamma\alpha(c_N c_1^\dagger + c_N c_1 + c_N^\dagger c_1^\dagger + c_N^\dagger c_1)\Big],\end{aligned} \tag{A8}$$

where the phase factor $s = (-1)^{N_p+1}$ depends on the total fermion number $N_p = \sum_j c_j^\dagger c_j$ and enforces parity sectors. Consequently the fermionic chain may obey either periodic ($c_{N+1} = c_1$) ; the $1/N$ corrections coming from the boundary term vanish in the thermodynamic limit. Introducing the Fourier transform

$$c_j = \frac{1}{\sqrt{N}}\sum_k e^{-ikj}c_k, \qquad c_j^\dagger = \frac{1}{\sqrt{N}}\sum_k e^{ikj}c_k^\dagger, \tag{A9}$$

(and using the half-integer momenta appropriate to the antiperiodic sector, $k = n\pi/N$ with $n = -(N-1), -(N-3), \ldots, (N-1)$), the bilinear Hamiltonian becomes

$$\begin{aligned}\hat{H} = &\sum_k \left[(2\cos k + 2\Gamma(\alpha-1)\sin k - 2h)\, c_k^\dagger c_k\right] + Nh \\ &+ \sum_k \left\{[\Gamma(\alpha+1) + i\gamma]\sin k\, c_{-k}c_k + \text{H.c.}\right\}.\end{aligned} \tag{A10}$$

This quadratic form can be written in Bogoliubov–de Gennes (BdG) notation as

$$\hat{H} = \sum_k \begin{pmatrix} c_k^\dagger & c_{-k}\end{pmatrix} \mathcal{H}_k \begin{pmatrix} c_k \\ c_{-k}^\dagger\end{pmatrix}, \tag{A11}$$

Diagonalization is achieved via the Bogoliubov transformation

$$b_k = u_k c_k + v_k e^{i\varphi_k} c_{-k}^\dagger, \qquad b_{-k} = u_k c_{-k} - v_k e^{i\varphi_k} c_k^\dagger, \tag{A12}$$

with real coefficients satisfying $u_k = u_{-k}$, $v_{-k} = -v_k$ and phases $\varphi_k = \varphi_{-k}$.The Hamiltonian becomes diagonal,

$$\hat{H} = \sum_k \varepsilon_k \left(b_k^\dagger b_k - \tfrac{1}{2}\right), \tag{A13}$$

Where the excitation spectrum ϵ_k is given by :

$$\epsilon_k = P_k + \sqrt{A_k^2 + B_k^2 + Q_k^2}, \tag{A14}$$

with

$$A_k = 2\Big[J\cos(k) - h\Big], \tag{A15}$$

$$B_k = 2J\,\delta\,\sin(k), \tag{A16}$$

$$P_k = 2\Gamma(\gamma-1)\sin(k), \tag{A17}$$

$$Q_k = 2\Gamma(\gamma+1)\sin(k). \tag{A18}$$

The Bogoliubov transformations introduce angles defined as :

$$\tan(2\theta_k) = \frac{2B_k Q_k}{Q_k^2 - B_k^2}, \quad \tan(2\Phi_k) = \mathrm{sgn}(k)\,\frac{\sqrt{B_k^2+Q_k^2}}{A_k}, \tag{A19}$$

In the thermodynamic limit, the ground state is formed by filling all negative-energy quasiparticle states:

$$b_k|\mathrm{GS}\rangle = 0 \quad \text{if } \varepsilon_k \geq 0, \qquad b_k^\dagger|\mathrm{GS}\rangle = 0 \quad \text{if } \varepsilon_k < 0, \tag{A20}$$

with the single-particle spectrum

$$\varepsilon_k = 2\sqrt{\Gamma^2(1+\alpha)^2\sin^2 k + (\cos k - h)^2 + \gamma^2\sin^2 k} - 2\Gamma(1-\alpha)\sin k \tag{A21}$$

In the thermodynamic limit the ground state is obtained by filling all modes with $\varepsilon_k < 0$ and leaving empty those with $\varepsilon_k \geq 0$. Equivalently, the ground state $|GS\rangle$ satisfies

$$b_k|GS\rangle = 0 \quad \text{for } \varepsilon_k \geq 0, \qquad b_k^\dagger|GS\rangle = 0 \quad \text{for } \varepsilon_k < 0, \tag{A22}$$

and the ground-state energy reads

$$E_0 = -\tfrac{1}{2}\sum_k |\varepsilon_k|. \tag{A23}$$

Appendix B: Critical lines

The critical points are determined by the condition that the excitation gap vanishes, namely $\varepsilon_k = 0$. Three distinct critical situations can be identified, depending on the sign of the combination $4\alpha\Gamma^2 + \gamma^2$. When $4\alpha\Gamma^2 + \gamma^2 > 0$, the critical mode occurs at $k_c = 0$, and the corresponding critical field is

$$h_{c,1} = 1.$$

When $4\alpha\Gamma^2 + \gamma^2 = 0$ with $h \leq 1$, the critical momentum is $k_c = \arccos h$, and the critical coupling parameter takes the value

$$\alpha_{c,1} = -\frac{\gamma^2}{4\Gamma^2}.$$

Finally, for $4\alpha\Gamma^2 + \gamma^2 < 0$, one can define another critical condition where the system becomes gapless. The corresponding critical field can be expressed as

$$h_{c,2} = \sqrt{1 - \gamma^2 - 4\Gamma^2\alpha}\,,$$

and the associated critical mode satisfies $k_c = \arccos(h_{c,2}^{-1})$. In the gapless region, which is enclosed by the last two critical conditions, the excitation spectrum ε_k contains two Fermi points, denoted by k_L and k_R. Defining

$$X = 4\alpha\Gamma^2 + \gamma^2,$$

these two Fermi points are given by

$$k_{L,R} = \arccos\left(h \pm \frac{\sqrt{(h^2-1)X + X^2}}{1-X}\right). \tag{B1}$$

As h approaches the critical value $h_{c,2}$, the two Fermi points merge into a single point at $\arccos(h_{c,2}^{-1})$. The critical exponents z (dynamical) and ν (correlation length) can be determined from the scaling relations $\Delta \sim (\lambda - \lambda_c)^{z\nu}$ and $\Delta(\lambda_c) \sim (k - k_c)^z$, where Δ denotes the spectral gap. At the critical field $h = h_{c,2}$, where $\cos k_c = h_{c,2}^{-1}$ and $\varepsilon(k_c) = 0$, an expansion of ε_k around k_c up to second order in $\delta k = k - k_c$ yields

$$\varepsilon(k_c + \delta k) = \left[\frac{\Gamma(1-\alpha)\cos^2 k_c}{2\sin k_c} + \frac{(h_{c,2}^{-1} - h_{c,2})^2}{2\Gamma\sin k_c(1-\alpha)}\right]\delta k^2, \tag{B2}$$

which indicates a quadratic dependence and thus $z = 2$. Expanding the energy gap near $h_{c,2}$ with $\delta h = h - h_{c,2}$, one obtains

$$\Delta \approx \varepsilon(k_c) = \frac{2(h_{c,2} - h_{c,2}^{-1})}{\Gamma(1-\alpha)\sin k_c}\,(h - h_{c,2}), \tag{B3}$$

implying $\nu z = 1$, which gives $\nu = \frac{1}{2}$ and $z = 2$. Near the critical field $h_{c,1} = 1$, for which $k_c = 0$, the dispersion relation can be expanded as

$$\varepsilon_k \approx 2\sqrt{\Gamma^2(1+\alpha)^2 + \gamma^2}\,|k| - 2\Gamma(1-\alpha)k, \tag{B4}$$

showing a linear dependence in k and therefore $z = 1$. The corresponding energy gap behaves as

$$\Delta = \varepsilon(k_c = 0) = 2|h-1| = 2(h - h_{c,1})^{\nu z}, \tag{B5}$$

which yields $\nu = 1$ and $z = 1$. Expanding the dispersion relation around $\alpha_{c,1} = -\gamma^2/(4\Gamma^2)$ with $\delta k = k - k_c$ (where $k_c = \arccos h$) gives

$$\varepsilon_k = \sqrt{1-h^2}\;\Gamma(1-\alpha_{c,1})\,(k-k_c)^2, \tag{B6}$$

leading again to $z = 2$. Finally, the gap near $\alpha_{c,1}$ behaves as

$$\Delta = \frac{4\Gamma\sin k_c}{1-\alpha_{c,1}}\,(\alpha - \alpha_{c,1}), \tag{B7}$$

which confirms that $\nu z = 1$.

Appendix C: Scaling, spectra and universality classes

Typically, one may introduce spatial and temporal characteristic scales that diverge as the control parameter λ approaches its critical value λ_c. The power-law divergence of these scales is encoded by the correlation-length exponent ν and the dynamical exponent z, which in turn allow the classification of transitions into universality classes. The low-energy behaviour controlling the critical properties is governed by the states in the vicinity of the momentum where the gap closes.

The dynamical exponent z relates energy and length scalings and can be read off from the spectral shape close to the gap-closing mode via $\Delta \sim (k-k_c)^z$, while the gap vanishes as $\Delta \sim (\lambda-\lambda_c)^{\nu z}$ when $\lambda \to \lambda_c$. Expanding at the critical line $h_{c,1}$ around the gap-closing momentum $k_c = 0$ yields the low-k form

$$\varepsilon_k \simeq 2\sqrt{\gamma^2+\Gamma^2(1+\alpha)^2}\,|k| - 2\Gamma(1-\alpha)\,k. \tag{C1}$$

This relativistic-like dispersion at the critical line $h_{c,1}$ implies a linear scaling in momentum and therefore $z = 1$. The gap close to $h_{c,1}$ is well approximated by

$$\Delta \simeq 2|h - h_{c,1}|, \tag{C2}$$

from which $\nu z = 1$ follows; hence the transition between phase I and phase II belongs to the two-dimensional Ising universality class with $\nu = 1$ and $z = 1$. On the boundary between the gapped phase II and the gapless phase III the spectrum closes at an incommensurate momentum $k_c = \arccos(h_{c,2}^{-1})$. An expansion around this momentum gives a quadratic dispersion of the form

$$\varepsilon_k \simeq \left[\frac{\Gamma(1-\alpha)\cos^2 k_c}{2\sin k_c} + \frac{(h_{c,2}^{-1}-h_{c,2})^2}{2\Gamma(1-\alpha)\sin k_c}\right](k-k_c)^2, \tag{C3}$$

which indicates $z = 2$. Expanding the gap near $h_{c,2}$ (taking $\delta h = h - h_{c,2}$) yields

$$\Delta \simeq \frac{2\big(h_{c,2}-h_{c,2}^{-1}\big)}{\Gamma(1-\alpha)\sin k_c}\,(h-h_{c,2}), \tag{C4}$$

so that $\nu z = 1$ and therefore $\nu = \frac{1}{2}$. These exponents ($\nu = \frac{1}{2}$, $z = 2$) identify the transition as belonging to the Lifshitz universality class, which here corresponds to the quantum criticality of free fermions. For the transition between phase I and the gapless phase III at the coupling threshold $\alpha_{c,1}$, the dispersion around the gap-closing momentum $k_c = \arccos h$ is again quadratic:

$$\varepsilon_k \simeq \sqrt{1-h^2}\,\Gamma(1-\alpha_{c,1})\,(k-k_c)^2, \tag{C5}$$

implying $z = 2$. The gap for α slightly above $\alpha_{c,1}$ scales as

$$\Delta \simeq \frac{4\Gamma\sin k_c}{1-\alpha_{c,1}}\,(\alpha-\alpha_{c,1}), \tag{C6}$$

which again yields $\nu z = 1$ and therefore places this transition in the Lifshitz universality class with $\nu = \frac{1}{2}$ and $z = 2$.

Appendix D: Thermal and Magnetic criticality

Since the ground state is invariably by the vacuum, the first excited state corresponds to a state occupied by a single fermion. Consequently, the energy gap is determined by the smallest of all ϵ_k values, expressed as:

$$\Delta = \min_k \epsilon_k. \tag{D1}$$

For the sake of simplicity, we shall consider the transverse-field Ising model (TFIM) with $\gamma = 1$. In this case, the dispersion relation reduces to:

$$\epsilon_k = \sqrt{h^2 + J^2 - 2hJ\cos k}, \tag{D2}$$

where g denotes the transverse field strength and J represents the coupling constant. Differentiating with respect to k, we obtain:

$$\frac{\partial \epsilon_k}{\partial k} = -\frac{Jh\sin k}{\epsilon_k} = 0, \tag{D3}$$

indicating that the extrema of ϵ_k occur at $k = 0$ or $k = \pi$. For $h > 0$, the minimum is located at $k = \pi$, whereas for $g < 0$, it shifts to $k = 0$. Evaluating the dispersion relation at these points yields:

$$\epsilon_{k=0} = |h - J|, \quad \epsilon_{k=\pi} = |h + J|. \tag{D4}$$

Focusing on the case where $h > 0$, we observe that the energy gap vanishes at the critical point:

$$h_c = J. \tag{D5}$$

This result demonstrates that the TFIM exhibits a phase transition at the same critical value h_c as the XX model. At this critical point, the gap closes entirely. However, in contrast to the XX model, the gap in the TFIM reopens as h exceeds h_c, signifying a distinct post-critical behavior.

$$\langle \hat{N} \rangle = \frac{L}{2\pi}\int_{-k_F}^{k_F} dk = \frac{L}{\pi}k_F = \frac{L}{\pi}\arccos\left(-\frac{h}{J}\right), \tag{D6}$$

with $k_F = \arccos(-h/J)$. Substituting this result into Eq. (D7), the magnetization becomes:

$$m = \begin{cases} -1 & \text{if } h/J < -1, \\ \frac{2}{\pi}\arccos\left(-\frac{h}{J}\right) - 1 & \text{if } -1 < h/J < 1, \\ 1 & \text{if } h/J > 1. \end{cases} \tag{D7}$$

This expression is illustrated in Fig.11-a, which depicts the magnetization of the XX model in its ground state as a function of the transverse field h/J.

As observed, the magnetization exhibits a kink at the critical points:

$$h_c = \pm J, \tag{D8}$$

marking the phase transition of the model. The derivative of the magnetization with respect to g, known as the susceptibility , is given by:

$$\chi = \frac{\partial m}{\partial h} = \begin{cases} 0 & \text{if } h/J < -1, \\ \frac{2/\pi}{\sqrt{J^2-h^2}} & \text{if } -1 < h/J < 1, \\ 0 & \text{if } h/J > 1, \end{cases} \tag{D9}$$

which diverges as h approaches h_c, as illustrated in Fig.11-b.

The dispersion relation is:

$$\epsilon_k = \sqrt{h^2 + J^2 - 2hJ\cos k} \tag{D10}$$

This represents the energy of fermionic quasiparticles in the system. The internal energy U for a system of N sites in one dimension, summing over all momentum modes k, is given by:

$$U = \sum_k \epsilon_k \langle n_k \rangle \tag{D11}$$

where $\langle n_k \rangle$ is the thermal occupation number for the fermionic quasiparticles, following the Fermi-Dirac distribution (adjusted for the quasiparticle vacuum):

$$\langle n_k \rangle = \frac{1}{e^{\beta\epsilon_k} + 1} \tag{D12}$$

Here, $\beta = 1/(k_B T)$, with k_B being the Boltzmann constant (often set to 1 in theoretical calculations for simplicity), and T is the temperature.In the thermodynamic limit ($N \to \infty$), the sum over k becomes an integral over the first Brillouin zone ($-\pi \leq k \leq \pi$) for a one-dimensional lattice:

$$U = \frac{N}{2\pi} \int_{-\pi}^{\pi} \epsilon_k \cdot \frac{1}{e^{\beta\epsilon_k} + 1}\, dk \tag{D13}$$

The factor $N/(2\pi)$ accounts for the density of states in k-space, as the number of k-points in $[-\pi, \pi]$ is N, and the spacing is $2\pi/N$.To find C_v illustrated in Fig.11-c, differentiate the internal energy with respect to temperature:

$$C_v = \frac{\partial U}{\partial T} \tag{D14}$$

Substitute U:

$$U = \frac{N}{2\pi} \int_{-\pi}^{\pi} \epsilon_k \cdot \frac{1}{e^{\beta\epsilon_k} + 1}\, dk \tag{D15}$$

Since $\beta = 1/(k_B T)$, we have $\frac{\partial \beta}{\partial T} = -\frac{1}{k_B T^2}$. Assuming $k_B = 1$ for simplicity (common in theoretical physics), $\beta = 1/T$, and $\frac{\partial \beta}{\partial T} = -\frac{1}{T^2}$.

Differentiate U with respect to T:

$$C_v = \frac{\partial U}{\partial T} = \frac{N}{2\pi} \int_{-\pi}^{\pi} \epsilon_k \cdot \frac{\partial}{\partial T} \left(\frac{1}{e^{\beta\epsilon_k} + 1} \right) dk \tag{D16}$$

Compute the derivative of the occupation number:

$$f(\epsilon_k) = \frac{1}{e^{\beta\epsilon_k} + 1} \tag{D17}$$

Thus:

$$C_v = \frac{N}{2\pi T^2} \int_{-\pi}^{\pi} \epsilon_k^2 \cdot \frac{e^{\beta\epsilon_k}}{(e^{\beta\epsilon_k} + 1)^2}\, dk \tag{D18}$$

This integral can be simplified by recognizing that:

$$\frac{e^{\beta\epsilon_k}}{(e^{\beta\epsilon_k} + 1)^2} = \frac{1}{e^{\beta\epsilon_k} + 1} \cdot \frac{e^{\beta\epsilon_k}}{e^{\beta\epsilon_k} + 1} = f(\epsilon_k)(1 - f(\epsilon_k)) \tag{D19}$$

So:

$$C_v = \frac{N}{2\pi T^2} \int_{-\pi}^{\pi} \epsilon_k^2 f(\epsilon_k)(1 - f(\epsilon_k))\, dk \tag{D20}$$

Due to the divergence of the specific heat near criticality, a system at a phase transition is capable of exchanging considerable amounts of heat, even under minimal temperature gradients. An analogous phenomenon may occur in our magnetic system. In the vicinity of the quantum critical point, the magnetic susceptibility—quantified as the derivative of the magnetization with respect to the transverse field—diverges. This signals an extreme sensitivity of the magnetization to even slight variations in the external field.

Appendix E: Correlation Functions

To evaluate the two-qubit correlation functions, we introduce the operators:

$$A_i = c_i^\dagger + c_i, \quad B_i = c_i^\dagger - c_i, \tag{E1}$$

where $c_i^\dagger$ and c_i denote the creation and annihilation operators at site i, respectively. It can be readily confirmed that these operators satisfy:

$$\{A_i, A_j\} = 2\delta_{ij}, \quad \{B_i, B_j\} = -2\delta_{ij}, \quad \{A_i, B_j\} = 0. \tag{E2}$$

The Pauli matrices are then expressed as:

$$\sigma_x^i = A_i \prod_{j=1}^{i-1} A_j B_j, \quad \sigma_y^i = iB_i \prod_{j=1}^{i-1} A_j B_j, \quad \sigma_z^i = A_i B_i. \tag{E3}$$

Using the Jordan-Wigner transformation, the x-component correlation function is:

$$\begin{aligned} G_{xx}^{i,j} &= \langle \sigma_x^i \sigma_x^j \rangle = \langle (\sigma_+^i + \sigma_-^i)(\sigma_+^j + \sigma_-^j) \rangle \\ &= \left\langle B_i \left(\prod_{n=i+1}^{j-1} A_n B_n \right) A_j \right\rangle \\ &= \langle B_i A_{i+1} B_{i+1} \cdots A_{j-1} B_{j-1} A_j \rangle. \end{aligned} \tag{E4}$$

Similarly, the y- and z-component correlations are:

$$G_{yy}^{i,j} = (-1)^{j-i} \langle A_i B_{i+1} A_{i+1} \cdots B_{j-1} A_{j-1} B_j \rangle, \tag{E5}$$

$$G_{zz}^{i,j} = \langle A_i B_i A_j B_j \rangle. \tag{E6}$$

The cross-correlations are:

$$G_{xy}^{i,j} = i \langle B_i A_{i+1} B_{i+1} \cdots A_{j-1} B_{j-1} B_j \rangle, \tag{E7}$$

$$G_{yx}^{i,j} = i \langle A_i A_{i+1} B_{i+1} \cdots A_{j-1} B_{j-1} A_j \rangle. \tag{E8}$$

By applying Wick's theorem , these correlations are expanded using contractions $\langle A_k A_l \rangle$, $\langle B_k B_l \rangle$, and $\langle B_k A_l \rangle$, yielding a Pfaffian representable as a $2r \times 2r$ antisymmetric determinant, where $r \equiv |j - i|$. Under reflection symmetry ($\Gamma = 0$), we have:

$$\langle A_k A_l \rangle = \delta_{kl}, \quad \langle B_k B_l \rangle = -\delta_{kl}, \tag{E9}$$

vanishing for $k \neq l$, reducing the Pfaffian to an $r \times r$ Toeplitz determinant. However, with broken reflection symmetry due to off-diagonal Γ interactions, and a non-positive excitation spectrum , $\langle A_k A_l \rangle$ and $\langle B_k B_l \rangle$ are finite for $k \neq l$ in the gapless phase, implying non-zero $\langle \sigma_x^i \sigma_y^j \rangle$ and $\langle \sigma_y^i \sigma_x^j \rangle$. The z-component correlation is decomposed as:

$$\begin{aligned} G_{zz}^{i,j} &= \langle B_i A_i \rangle \langle B_j A_j \rangle - \langle B_j A_i \rangle \langle B_i A_j \rangle \\ &\quad - \langle A_i A_j \rangle \langle B_i B_j \rangle, \end{aligned} \tag{E10}$$

where the final term is often incorrectly neglected. For nearest-neighbor correlations ($r = 1$):

$$\begin{aligned} G_{xx}^{i,i+1} &= \langle B_i A_{i+1} \rangle, \quad G_{yy}^{i,i+1} = -\langle A_i B_{i+1} \rangle, \\ G_{xy}^{i,i+1} &= i\langle B_i B_{i+1} \rangle, \quad G_{yx}^{i,i+1} = i\langle A_i A_{i+1} \rangle, \\ G_{zz}^{i,i+1} &= \langle A_i B_i A_{i+1} B_{i+1} \rangle \\ &= \langle \sigma_z^i \rangle \langle \sigma_z^{i+1} \rangle - \langle \sigma_x^i \sigma_x^{i+1} \rangle \langle \sigma_y^i \sigma_y^{i+1} \rangle \\ &\quad + \langle \sigma_x^i \sigma_y^{i+1} \rangle \langle \sigma_y^i \sigma_x^{i+1} \rangle. \end{aligned} \tag{E11}$$

Non vanishing cross-correlations introduce nontrivial effects in systems lacking reflection symmetry, fostering a gapless phase with quasi-long-range order. Since the Hamiltonian is quadratic in fermionic operators, complete knowledge of the matrix G allows for the direct computation of zero-temperature expectation values of the Hamiltonian. Additionally, the action of any operator that is quadratic in the creation $\hat{b}^{(\dagger)}$ and annihilation operators $\hat{b}$ preserves the Gaussian character of the state. The nearest-neighbour two-point correlators exhibit sharp changes when the system crosses quantum critical points separating gapless and gapped phases. For example, at $h = 0.50$ increasing the interaction-range exponent α causes the leading nearest-neighbour correlation to switch from a positive G_1^{yx} to a negative G_1^{xx}, signalling a quantum phase transition from the gapless spiral phase into a gapped ferromagnetic (FM) phase. By contrast, the dominant correlations G_1^{zz} for $h = 1.17$ are consistent with phase II being paramagnetic (PM). Comparable behaviour for $\alpha = 0.50$ is displayed in [110, 140]: across $h_{c,1}$ the dominant nearest-neighbour correlator changes from negative G_1^{xx} to positive G_1^{zz}, and the first derivative of G_1^{xx} develops a pronounced peak at $h_{c,1}$. Finite-size scaling of the field-derivative of G_1^{xx} reveals a logarithmic singularity at the second-order critical point. Numerically we find

$$\left(\frac{\partial G_1^{xx}}{\partial h} \right)_{\max} = a_G \ln N + c_3, \tag{E12}$$

$$\frac{\partial G_1^{xx}}{\partial h} = b_G \ln |h - h_c| + c_4, \tag{E13}$$

with fitted coefficients $a_G = 0.2789 \pm 0.0045$, $b_G = -0.2811 \pm 0.0001$, $c_3 = 0.1758$ and $c_4 = 0.0265$. From these amplitudes one can estimate the correlation-length exponent via

$$\nu \approx \left| \frac{a_G}{b_G} \right| = 0.9922 \pm 0.0209,$$

in excellent agreement with the value obtained from the second derivative of the ground-state energy density. The FM region supports long-range order (LRO) interaction , whereas the PM regime does not. We also observe that in the gapped phases the magnitudes of G_1^{xy} and G_1^{yx} coincide, while they become asymmetric in the gapless regime. This suggests that the quantity

$$\Delta_\chi \equiv \left| G_1^{xy} \right| - \left| G_1^{yx} \right|$$

serves as an effective order parameter to detect the spiral phase in the XY–Gamma model. To assess whether genuine long-range order exists inside the gapless spiral region, we computed the vector-chiral correlator difference

$$\left| G_r^{xy} \right| - \left| G_r^{yx} \right|$$

for several separations r ; absolute values are taken to remove sign-ambiguities arising from the Pfaffian evaluation. In the gapped phases the difference vanishes (since $G_r^{xy} = G_r^{yx}$), while it remains finite in the spiral regime. As r increases the correlation difference decays in an oscillatory manner approximately as $r^{-1/2}$, indicating quasi-long-range order of an incommensurate spiral. To characterise the spiral further we examined four-site (dimer) correlations. The dimer correlator between sites j and $j + r$ is defined by

$$D_{j,j+r} = \langle \kappa_j \kappa_{j+r} \rangle - \langle \kappa_j \rangle \langle \kappa_{j+r} \rangle, \tag{E14}$$

where the z-component of the vector-chiral operator is

$$\kappa_j = \big(\boldsymbol{\sigma}_j \times \boldsymbol{\sigma}_{j+1} \big)_z. \tag{E15}$$

Equations (E14)–(E15) were used to probe dimer and chiral correlations (for more details consult [62]) . The two adjacent dimers one finds the relation

$$\langle \kappa_i \kappa_{i+1} \rangle = \langle B_i B_{i+2} \rangle, \tag{E16}$$

where B_i denotes the appropriate two-spin operator defined in the text. For dimers separated by a distance $r \equiv j - i > 1$ the dimer–dimer correlator can be written in the form

$$\begin{aligned} \langle \kappa_i \kappa_j \rangle &= \langle B_i B_j \rangle \langle B_{i+1} B_{j+1} \rangle - \langle B_i B_{i+1} \rangle \langle B_j B_{j+1} \rangle \\ &\quad - \langle B_i B_{j+1} \rangle \langle B_{i+1} B_j \rangle, \end{aligned} \tag{E17}$$

which follows from the decomposition of the four-point function into products of two-point building blocks. Importantly, nonzero cross-correlations of the type appearing in Eq. (E17) produce nontrivial effects whenever reflection symmetry is broken. Such correlations are a hallmark of the gapless regime and are responsible for the emergence of quasi-long-range incommensurate (spiral) order in the model.

Appendix F: Two-level decoupling and mapping to an LZSM problem

For the time-dependent Hamiltonian $H\big(h(t)\big)$ the unitary dynamics couples, for each momentum k, only the pair of ba-

sis states $|0_k, 0_{-k}\rangle$ and $|1_k, 1_{-k}\rangle$. Consequently, the full evolution factorizes into N independent two-dimensional problems, one per k-mode [141]. Introducing the Bogoliubov amplitudes $u_k(t)$ and $v_k(t)$, the mode dynamics can be written as a 2×2 matrix Schrödinger equation

$$i\frac{d}{dt}\begin{pmatrix} u_k \\ v_k \end{pmatrix} = H_k(t)\begin{pmatrix} u_k \\ v_k \end{pmatrix}, \tag{F1}$$

where $H_k(t)$ is the two-level Hamiltonian with $h = h(t)$.By performing the change of variables :

$$t' = \frac{\Delta_k\big(t_k - h + \delta t\big)}{\delta}, \tag{F2}$$

the evolution (F1) is mapped onto a standard Landau–Zener–Stückelberg–Majorana (LZSM) form [142, 143],

$$i\frac{d}{dt'}\begin{pmatrix} u_k \\ v_k \end{pmatrix} = \begin{pmatrix} -\Omega_k t' & 1 \\ 1 & \Omega_k t' \end{pmatrix}\begin{pmatrix} u_k \\ v_k \end{pmatrix}, \tag{F3}$$

with $\Omega_k = \delta/\Delta_k^2$. The general solution of (F3) can be expressed in terms of parabolic-cylinder (Weber) functions $D_\nu(z)$ [144, 145]. A convenient form for the coefficients is

$$v_k(t') = a\, D_{-s-1}(-iz) + b\, D_{-s-1}(iz), \tag{F4a}$$

$$u_k(t') = \left(\Omega_k t' - 2i\frac{\partial}{\partial t'}\right) v_k(t'), \tag{F4b}$$

where

$$s = \frac{1}{4i\Omega_k}, \qquad z = \sqrt{\Omega_k}\, t'\, e^{i\pi/4}, \tag{F5}$$

and the complex constants a and b are fixed by the initial values $u_k(t_i)$ and $v_k(t_i)$. The many-body state then factorizes into a product of k-mode states,

$$|\Psi(t)\rangle = \prod_k |\psi_k(t)\rangle, \tag{F6}$$

with:

$$|\psi_k(t)\rangle = u_k(t)\,|0_k, 0_{-k}\rangle + v_k(t)\,|1_k, 1_{-k}\rangle, \tag{F7}$$

and the time dependence understood through $t' = t'(t)$. It is useful to introduce the instantaneous eigenvectors of $H_k(t)$ [146, 147],

$$|\varphi_k^{\pm}(t)\rangle = \bar{u}_k\big(h(t)\big)\,|0_k, 0_{-k}\rangle \pm \bar{v}_k\big(h(t)\big)\,|1_k, 1_{-k}\rangle, \tag{F8}$$

where $\bar{u}_k(h) = \cos\big(\theta_k(h)/2\big)$, $\bar{v}_k(h) = \sin\big(\theta_k(h)/2\big)$, and $\theta_k(h) = \arctan\big(\Delta_k/(h - t_k)\big)$ is the Bogoliubov angle for chemical potential h. The occupation probability of the instantaneous eigenstate during evolution is therefore

$$P_k(t) = \big|\langle\varphi_k^{\pm}(t)|\psi_k(t)\rangle\big|^2 = \big|\bar{u}_k\big(h(t)\big)\,u_k(t) + \bar{v}_k\big(h(t)\big)\,v_k(t)\big|^2. \tag{F9}$$

Substituting the explicit solutions (F4a)–(F4b) into (F9) yields an exact (but rather involved) analytic expression for $P_k(t)$ in terms of parabolic-cylinder functions. A simpler and physically transparent approximation emerges in the slow-driving limit, $\delta \to 0$, where the final protocol duration $\tau = |h_f - h_i|/\delta \to \infty$. To leading nontrivial order in this adiabatic regime the transition probability takes the celebrated LZSM form

$$P_k \simeq 1 - \exp\Big(-\frac{\pi\Delta_k^2}{\delta}\Big) + \mathcal{O}(\delta^2). \tag{F10}$$

Although corrections of order δ^2 formally dominate for fixed Δ_k as $\delta \to 0$, when the system traverses the critical region the dynamics is governed by the soft modes with small Δ_k. For thermodynamic observables the exponentially small Landau–Zener contribution in (F10) therefore outweighs the analytic $\mathcal{O}(\delta^2)$ terms and controls the nonadiabatic response.

$$Q_c = \langle\hat{H}(t_f)\rangle_{\rho_C}(1 - 2P_k) - \langle\hat{H}(t_f)\rangle_{\rho_B}, \tag{F11}$$

$$Q_h = \langle\hat{H}(t_i)\rangle_{\rho_A}(1 - 2P_k) - \langle\hat{H}(t_i)\rangle_{\rho_D}. \tag{F12}$$

In this work we employ a driving time-scale for which the adiabatic approximation is valid; consequently, in the long-time (quasistatic) adiabatic limit we set $P_k = 1$ for all modes k, thereby neglecting nonadiabatic transitions.

[1] D. E. Winterbone and A. Turan, Advanced Thermodynamics for Engineers, Butterworth-Heinemann, 2015.

[2] S. Deffner and S. Campbell, Thermodynamics of Quantum Systems, Quantum Thermodynamics, Morgan Claypool Publishers (2019).

[3] P. Strasberg (2021) Quantum stochastic thermodynamics: foundations and selected applications, Oxford University Press, 2022.

[4] J. P. Pérez, Thermodynamique: fondements et applications: avec 250 exercices et problèmes résolus, Dunod, 2001.

[5] H. E. Scovil and E. O. Schulz-DuBois, Three-level masers as heat engines, Phys. Rev. Lett, **2** (1959) 262.

[6] E. Latifah and A. Purwanto, Quantum Heat Engines; Multiple-State 1D Box System, Journal of Modern Physics, **4** (2013) 1091–1098.

[7] C. M. Bender, D. C. Brody, and B. K. Meister, Entropy and temperature of a quantum Carnot engine, Proceedings of the Royal Society of London. Series A: Mathematical, Physical and Engineering Sciences, **458** (2002) 1519-1526.

[8] C. M. Bender, D. C. Brody, and B. K. Meister, Quantum mechanical Carnot engine, J. Phys. A: Math. Gen. **33** (2000) 4427.

[9] A. Solfanelli, M. Falsetti, and M. Campisi, Nonadiabatic single-qubit quantum Otto engine, Phys. Rev. B. **101**, 054513 (2020).

[10] G. Piccitto, M. Campisi, and D. Rossini, The Ising critical quantum Otto engine, New Journal of Physics, **24** (2022) 103023.

[11] Y. Yin, Optimal power and efficiency of quantum Stirling heat engines, Eur. Phys. J. Plus, **132** (2017) 45.

[12] Y. Yin, L. Chen, and F. Wu, Performance of quantum Stirling heat engine with numerous copies of extreme relativistic particles confined in 1D potential well, Physica A, **503** (2018) 58.

[13] Deny Pra Setyo, Eny Latifah, Hari Wisodo, and Arif Hidayat, Quantum Relativistic Diesel Engine with Single Massless Fermion in 1 Dimensional Box System, Jurnal Penelitian Fisika dan Aplikasinya (JPFA), **8**, 1 (2018).

[14] Deny Pra Setyo and Eny Latifah, Quantum Otto Engine based on Multiple-State Single Fermion in 1D Box System, IOP Conf. Series: Journal of Physics: Conf. Series, **1093** (2018) 012030.

[15] Agus Purwanto, Heru Sukamto, Bintoro Anang Subagyo, and Muhammad Taufiqi, Two Scenarios on the Relativistic Quantum Heat Engine, Journal of Applied Mathematics and Physics, **4** (2016) 1344–1353.

[16] P. A. Camati, J. F. Santos, and R. M. Serra, Coherence effects in the performance of the quantum Otto heat engine, Phys. Rev. A, **99** (2019) 062103.

[17] Q. Bouton, J. Nettersheim, S. Burgardt, D. Adam, E. Lutz, and A. Widera, A quantum heat engine driven by atomic collisions, Nat. Commun, **12** (2021) 2063.

[18] E. Muñoz and F. J. Peña, Quantum heat engine in the relativistic limit: The case of a Dirac particle, Phys. Rev. E, **86** (2012) 061108.

[19] P. Chattopadhyay and G. Paul, Relativistic quantum heat engine from uncertainty relation standpoint, Scientific reports, **9** (2019) 16967.

[20] V. R. Arezzo, D. Rossini, and G. Piccitto, Many-body quantum heat engines based on free fermion systems, Phys. Rev. B, **109** (2024) 224309.

[21] A. El Makouri, A. Slaoui, and R. A. Laamara, Quantum unital Otto heat engines: Using Kirkwood–Dirac quasi-probability for the engine's coherence to stay alive, Annals of Physics, **473** (2025) 169889.

[22] A. El Makouri, A. Slaoui, and R. Ahl Laamara, Monitored nonadiabatic and coherent-controlled quantum unital Otto heat engines: First four cumulants, Phys. Rev. E, **108** (2023) 044114.

[23] N. Ranabhat, and M. Collura, Thermalization of long range Ising model in different dynamical regimes: A full counting statistics approach, SciPost Physics Core, **7** (2024) 017.

[24] B. Amghar, A. Slaoui, J. Elfakir, and M. Daoud, Geometrical, topological, and dynamical description of N interacting spin-s particles in a long-range Ising model and their interplay with quantum entanglement, Phys. Rev. A, **107** (2023) 032402.

[25] A. Lerose, B. Žunkovič, A. Silva, and A. Gambassi, Quasilocalized excitations induced by long-range interactions in translationally invariant quantum spin chains, Phys. Rev. B, **99** (2019) 121112.

[26] G. Piccitto, B. Žunković, and A. Silva, Dynamical phase diagram of a quantum Ising chain with long-range interactions, Phys. Rev. B, **100** (2019) 180402.

[27] G. Piccitto and A. Silva, Crossover from fast to slow dynamics in a long-range interacting Ising chain, Journal of Statistical Mechanics: Theory and Practice, **2019** (2019) 094017.

[28] V. Mukherjee and U. Divakaran, Many-body quantum thermal machines, J. Phys.: Condens. Matter, **33** (2021) 454001.

[29] L. M. Cangemi, C. Bhadra, and A. Levy, Quantum engines and refrigerators, Physics Reports, **1087** (2024) 1-71.

[30] J. Jaramillo, M. Beau, and A. del Campo, Quantum supremacy of many-particle thermal machines, New J. Phys, **18** (2016) 075019.

[31] R. S. Watson, and K. V. Kheruntsyan, An interaction-driven quantum many-body engine enabled by atom-atom correlations, arXiv preprint arXiv:2308.05266, (2023).

[32] N. Y. Halpern, C. D. White, S. Gopalakrishnan, and G. Refael, Quantum engine based on many-body localization, Phys. Rev. B, **99** (2019) 024203.

[33] F. Carollo, F. M. Gambetta, K. Brandner, J. P. Garrahan, and I. Lesanovsky, Nonequilibrium quantum many-body rydberg atom engine, Phys. Rev. Lett, **124** (2020) 170602.

[34] T. Zhang, Four-level entangled quantum heat engines, Phys. Rev. A, **75** (2007) 062102.

[35] E. Muñoz and F. J. Peña, Magnetically driven quantum heat engine, Phys. Rev. E, **89** (2014) 052107.

[36] L. Mashhor, M. Y. Abd-Rabbou, A.-A. A. Yaya, M. Abdel-Aty and A.-S. F. Obada, "Quantum Otto and Carnot thermal machines powered by two two-level atoms enveloped by QED-cavity,"

[37] G. Procopio, C. Pezzotti, and M. Giona, "Ergodicity breaking in well-behaved generalized Langevin equations," Phys. Rev. E **111**, 034106 (2025). DOI: 10.1103/PhysRevE.111.034106.

[38] F. Altintas, "Irreversible quantum Carnot cycle and its comparison with quantum Otto cycle," *Physics Letters A*, vol. 533, Art. no. 130212, 15 February 2025. doi:10.1016/j.physleta.2024.130212.

[39] D. Bitko, T.F. Rosenbaum, G. Aeppli, Quantum critical behavior for a model magnet, *Phys. Rev. Lett.* **77** (1996) 940.

[40] R. Coldea, D.A. Tennant, E.M. Wheeler, E. Wawrzynska, D. Prabhakaran, M. Telling, K. Habicht, P. Smeibidl, K. Kiefer, Quantum criticality in an Ising chain: Experimental evidence for emergent E8 symmetry, *Science* **327** (2010) 177.

[41] Y. Cui, H. Zou, N. Xi, Z. He, Y.X. Yang, L. Shu, G.H. Zhang, Z. Hu, T. Chen, R. Yu, J. Wu, W. Yu, Quantum criticality of the Ising-like screw chain antiferromagnet $SrCo_2V_2O_8$ in a transverse magnetic field, *Phys. Rev. Lett.* **123** (2019) 067203.

[42] A.J. Neer, J. M.-Guerrero, J.E. So, B.C. Melot, K.A. Ross, et al., Ising-like antiferromagnetism on the octahedral sublattice of a cobalt-containing garnet and the potential for quantum criticality, *Phys. Rev. B* **95** (2017) 144419.

[43] A.A. Zvyagin, Generalizations of exactly solvable quantum spin models, *Phys. Rev. B* **101** (2020) 094403.

[44] D. Takikawa, Topological phase transition to Abelian anyon phases due to off-diagonal exchange interaction in the Kitaev spin liquid state, *Phys. Rev. B* **102** (2020) 174414.

[45] I. Dzyaloshinsky, A thermodynamic theory of weak ferromagnetism of antiferromagnetics, *J. Phys. Chem. Solids* **4** (1958) 241.

[46] T. Moriya, Anisotropic superexchange interaction and weak ferromagnetism, *Phys. Rev.* **120** (1960) 91.

[47] S. Kim, K. Ueda, G. Go, P.-H. Jang, et al., Correlation of the Dzyaloshinskii–Moriya interaction with Heisenberg exchange and orbital asphericity, *Nat. Commun.* **9** (2018) 1648.

[48] S. Mühlbauer, B. Binz, F. Jonietz, C. Pfleiderer, A. Rosch, A. Neubauer, R. Georgii, P. Böni, Skyrmion lattice in a chiral magnet, *Science* **323** (2009) 915–919.

[49] H.-S. Kim, H.-Y. Kee, Crystal structure and magnetism in α-$RuCl_3$: An *ab initio* study, *Phys. Rev. B* **93** (2016) 155143.

[50] L. Janssen, E.C. Andrade, M. Vojta, Magnetization processes of zigzag states on the honeycomb lattice: Identifying spin models for α-$RuCl_3$ and Na_2IrO_3, *Phys. Rev. B* **96** (2017) 064430.

[51] W. Wang, Z.-Y. Dong, S.-L. Yu, J.-X. Li, Theoretical investigation of magnetic dynamics in α-$RuCl_3$, *Phys. Rev. B* **96** (2017) 115103.

[52] D. Takikawa, S. Fujimoto, Impact of off-diagonal exchange interactions on the Kitaev spin-liquid state of α-$RuCl_3$, *Phys. Rev. B* **99** (2019) 224409.

[53] I.O. Ozel, C.A. Belvin, E. Baldini, I. Kimchi, S. Do, K.-Y. Choi, N. Gedik, Magnetic field-dependent low-energy magnon dynamics in α-$RuCl_3$, *Phys. Rev. B* **100** (2019) 085108.

[54] R.L. Smit, S. Keupert, O. Tsyplyatyev, P.A. Maksimov, A.L. Chernyshev, P. Kopietz, Magnon damping in the zigzag phase of the Kitaev-Heisenberg-Γ model on a honeycomb lattice, *Phys. Rev. B* **101** (2020) 054424.

[55] S. Ducatman, Magnetic structure and excitation spectrum of the hyperhoneycomb Kitaev magnet β-Li_2IrO_3, *Phys. Rev. B* **97** (2018) 125125.

[56] I. Rousochatzakis, Magnetic field induced evolution of intertwined orders in the Kitaev magnet β-Li_2IrO_3, *Phys. Rev. B* **97** (2018) 174423.

[57] J.G. Rau, E.K.-H. Lee, H.-Y. Kee, Generic spin model for the honeycomb iridates beyond the Kitaev limit, *Phys. Rev. Lett.* **112** (2014) 077204.

[58] T. Okubo, K. Shinjo, Y. Yamaji, N. Kawashima, S. Sota, T. Tohyama, M. Imada, Ground-state properties of Na_2IrO_3 determined from an *ab initio* Hamiltonian and its extensions containing Kitaev and extended Heisenberg interactions, *Phys. Rev. B* **96** (2017) 054434.

[59] R. Yadav. Large off-diagonal exchange couplings and spin liquid states in C_3-symmetric iridates, *Phys. Rev. B* **100** (2019) 144422.

[60] P. Lampen-Kelley. Destabilization of magnetic order in a dilute Kitaev spin liquid candidate, *Phys. Rev. Lett.* **119** (2017) 237203.

[61] Z.-A. Liu. Lifshitz phase transitions in a one-dimensional Γ model, *Phys. Rev. E* **102** (2020) 032127.

[62] Kheiri,. (2024). Information propagation in one-dimensional XY-Γ chains. 109. 10.1103/PhysRevB.109.134303.

[63] G. B. Mbeng. The quantum Ising chain for beginners, SciPost Phys. Lect. Notes, (2024) 82.

[64] E. Lieb, T. Schultz and D. Mattis, Two soluble models of an antiferromagnetic chain, Annals of Physics, **16** (1961) 407-466.

[65] T. Koffel .Entanglement entropy for the long range ising chain in a transverse field, Phys. Rev. Lett, **109** (2012) 267203.

[66] F. Iglói, Z. Szatmári, and Y.-C. Lin, Entanglement entropy with localized and extended interface defects, Phys. Rev. B **80**, 024405 (2009).

[67] I. Peschel, Calculation of reduced density matrices from correlation functions, J. Phys. A: Math. Gen. **36**, L205 (2003).

[68] P. Calabrese and J. Cardy, Entanglement entropy and quantum field theory, J. Stat. Mech.: Theory Exp. (2004) P06002.

[69] P. Calabrese and J. Cardy, Evolution of entanglement entropy in one-dimensional systems, J. Stat. Mech.: Theory Exp. (2005) P04010.

[70] M. B. Hastings, An area law for one-dimensional quantum systems, J. Stat. Mech.: Theory Exp. (2007) P08024.

[71] J. Eisert, M. Cramer, and M. B. Plenio, Area laws for the entanglement entropy, Rev. Mod. Phys. **82**, 277 (2010).

[72] M. Mehboudi.Thermometry Precision in Strongly Correlated Ultracold Lattice Gases.https://arxiv.org/pdf/1501.03095(2015)

[73] A. D'Abbruzzo and D. Rossini, Self-consistent microscopic derivation of Markovian master equations for open quadratic quantum systems, Phys. Rev. A 103, 052209 **50** (2021).

[74] A. Hminat, A. Slaoui, B. Amghar, and R. Ahl Laamara, Multiparticle quantum heat engine: Exploring the impact of criticality on efficiency, Phys. Rev. E **112**, 044104 (2025). https://doi.org/10.1103/qyby-5yvg.

[75] Dorner R, Goold J, Cormick C, Paternostro M and Vedral V 2012 Phys. Rev. Lett. 109 160601 URL https://doi.org/10.1103/PhysRevLett.109.160601

[76] Hecht, M. O. Ramsey interferometry for enhanced quantum sensing in decohering systems. *Nature Communications*, Open Access, 29 April 2025.

[77] Daly. Prospects for ultralow-mass nuclear magnetic resonance using spin defects in hexagonal boron nitride. *arXiv:quant-ph*, 25 April 2025.

[78] Ismail. Quantum dynamics in complex systems. *The European Physical Journal D*, 12 February 2025.

[79] A.Slaoui.Comparative study of local quantum Fisher information and local quantum uncertainty in Heisenberg XY model-Physics Letters A, 2019

[80] A. Hminat, A. Slaoui, R. Ahl Laamara, and M. Telmini, Hermitian vs non-Hermitian quantum thermometry, arXiv:2509.10840 (September 2025). DOI: 10.48550/arXiv.2509.10840. License: CC0.

[81] M. Campisi and R. Fazio, The power of a critical heat engine, Nat. Commun. **7** (2016) 11895.

[82] Zi-An , Quantum criticality and correlations in the Ising-Gamma chain, Physica A: Statistical Mechanics and its Applications, Volume 579, 2021, 126122, ISSN 0378-4371, https://doi.org/10.1016/j.physa.2021.126122.

[83] Fusco L, 2014 Phys. Rev. X 4 031029 URL https://doi.org/10.1103/PhysRevX.4. 031029

[84] P. Pfeuty, "The one-dimensional Ising model with a transverse field," Ann. Phys. **57**, 79–90 (1970). Received July 14, 1969.

[85] J. H. H. Perk and H. Au-Yang, "New results for the correlation functions of the Ising model and the transverse Ising chain," J. Stat. Phys. **135**, 599–619 (2009). DOI: 10.1007/s10955-009-9758-5. arXiv:0901.1931.

[86] S. Sachdev, "Quantum phase transitions," Physics World **12**(4), 33 (1999). DOI: 10.1088/2058-7058/12/4/23.

[87] G. O. Gomes, L. Squillante, A. C. Seridonio, A. Ney, R. E. Lagos, and M. de Souza, "Magnetic Grüneisen parameter for model systems," Phys. Rev. B **100**, 054446 (2019). DOI: 10.1103/PhysRevB.100.054446.

[88] S. L. Sondhi, S. M. Girvin, J. P. Carini, and D. Shahar, "Continuous quantum phase transitions," Rev. Mod. Phys. **69**, 315–333 (1997). DOI: 10.1103/RevModPhys.69.315.

[89] K.-W. Sun, C. Wang, and Q.-H. Chen, "Heat transport in an open transverse-field Ising chain," EPL (Europhys. Lett.) **92**(2), 24002 (2010). DOI: 10.1209/0295-5075/92/24002.

[90] M. Vogl, G. Schaller, and T. Brandes, "Criticality in transport through the quantum Ising chain," Phys. Rev. Lett. **109**, 240402 (2012). DOI: 10.1103/PhysRevLett.109.240402. arXiv:1208.5989.

[91] L. Zhu, M. Garst, A. Rosch, and Q. Si, "Universally diverging Grüneisen parameter and the magnetocaloric effect close to quantum critical points," Phys. Rev. Lett. **91**, 066404 (2003). DOI: 10.1103/PhysRevLett.91.066404. arXiv:cond-mat/0212335.

[92] A. Purkayastha, "Green–Kubo formula for general open quantum systems and open to closed system crossover," arXiv:1712.01068 (Dec 2017). DOI: 10.48550/arXiv.1712.01068.

[93] L. M. Cangemi, C. Bhadra, and A. Levy, "Quantum Engines and Refrigerators," arXiv:2302.00726 (Feb 2023). DOI: 10.48550/arXiv.2302.00726. License: CC BY 4.0.

[94] J. Dziarmaga, "Dynamics of a quantum phase transition and relaxation to a steady state," Adv. Phys. **59**(6), 1063–1189 (2010). DOI: 10.1080/00018732.2010.514702. arXiv:0912.4034.

[95] M. E. Fisher and M. N. Barber, "Scaling theory for finite-size effects in the critical region," Phys. Rev. Lett. **28**, 1516–1519 (1972). DOI: 10.1103/PhysRevLett.28.1516.

[96] M. Campostrini, A. Pelissetto, and E. Vicari, "Finite-size scaling at quantum transitions," Phys. Rev. B **89**, 094516 (2014). DOI: 10.1103/PhysRevB.89.094516. Preprint: arXiv:1401.0788.

[97] J. P. S. Peterson *et al.*, "Experimental Characterization of a Spin Quantum Heat Engine," Phys. Rev. Lett. **123**, 240601 (2019). DOI: 10.1103/PhysRevLett.123.240601. Preprint: arXiv:1803.06021.

[98] M. Vogl, G. Schaller, and T. Brandes, "Criticality in transport through the quantum Ising chain," Phys. Rev. Lett. **109**, 240402 (2012). DOI: 10.1103/PhysRevLett.109.240402. arXiv:1208.5989.

[99] E. Barouch and B. M. McCoy, "Statistical mechanics of the XY model. II. Spin-correlation functions," Phys. Rev. A **3**, 786–804 (1971). DOI: 10.1103/PhysRevA.3.786.

[100] J. H. H. Perk and H. Au-Yang, "New results for the correlation functions of the Ising model and the transverse Ising chain," J. Stat. Phys. **135**(4), 599–619 (2009). DOI: 10.1007/s10955-009-9758-5. arXiv:0901.1931.

[101] J. Dziarmaga, "Dynamics of a quantum phase transition and relaxation to a steady state," Adv. Phys. **59**(6), 1063–1189 (2010). DOI: 10.1080/00018732.2010.514702. arXiv:0912.4034.

[102] C. Purkait, S. Chand, and A. Biswas, "Anisotropy-assisted thermodynamic advantage of a local-spin quantum thermal machine," Phys. Rev. E **109**, 044128 (2024). DOI: 10.1103/PhysRevE.109.044128. Preprint: arXiv:2309.04757.

[103] S. Zanker, I. Schwenk, J.-M. Reiner, J. Leppäkangas, and M. Marthaler, "Analyzing the spectral density of a perturbed analog quantum simulator using Keldysh formalism," Phys. Rev. B **97**, 214301 (2018). DOI: 10.1103/PhysRevB.97.214301. arXiv:1705.02325.

[104] B. Bruognolo, A. Weichselbaum, J. von Delft, and M. Garst, "Dynamic structure factor of the spin-1/2 XXZ chain in a transverse field," Phys. Rev. B **94**, 085136 (2016). DOI: 10.1103/PhysRevB.94.085136. arXiv:1606.03294.

[105] P. Laurell, G. Alvarez, and E. Dagotto, "Spin dynamics of the generalized quantum spin compass chain," Phys. Rev. B **107**, 104414 (2023). DOI: 10.1103/PhysRevB.107.104414. arXiv:2210.00357.

[106] R. Cole, F. Pollmann, and J. J. Betouras, "Entanglement scaling and spatial correlations of the transverse-field Ising model with perturbations," Phys. Rev. B **95**, 214410 (2017). DOI: 10.1103/PhysRevB.95.214410. arXiv:1702.02664.

[107] M. Schmitt and M. Heyl, "Quantum dynamics in transverse-field Ising models from classical networks," SciPost Phys. **4**(2), 013 (2018). DOI: 10.21468/SciPostPhys.4.2.013. arXiv:1707.06656.

[108] H.-Q. Shi and H.-Q. Zhang, "Measuring Rényi Entropy in Neural Network Quantum States," Preprint: arXiv:2308.05513 (2023).

[109] S. Khetrapal and E. T. M. Pedersen, "Mutual information scrambling in an Ising spin chain," Phys. Rev. B **111**, 014439 (2025). DOI: 10.1103/PhysRevB.111.014439. arXiv:2402.13558.

[110] M. Asadian, S. Ahadpour, and F. Mirmasoudi, "Quantum correlated heat engine in XY chain with Dzyaloshinskii–Moriya interactions," Sci. Rep. **12**, 7081 (2022). DOI: 10.1038/s41598-022-11146-3.

[111] R. Jafari, M. Kargarian, A. Langari, and M. Siahatgar, "Phase diagram and entanglement of the Ising model with Dzyaloshinskii–Moriya interaction," Phys. Rev. B **78**, 214414 (2008). DOI: 10.1103/PhysRevB.78.214414.

[112] L.-M. Zhao and G.-F. Zhang, "Entangled quantum Otto heat engines based on two-spin systems with the Dzyaloshinskii–Moriya interaction," Preprint: arXiv:1708.05804 (2017). DOI: 10.48550/arXiv.1708.05804.

[113] G.-F. Zhang, "Entangled quantum heat engines based on two two-spin systems with Dzyaloshinskii–Moriya anisotropic antisymmetric interaction," Eur. Phys. J. D **49**(1), 123–128 (2008). DOI: 10.1140/epjd/e2008-00133-0.

[114] M. Kargarian, R. Jafari, and A. Langari, "Dzyaloshinskii–Moriya interaction and anisotropy effects on the entanglement of the Heisenberg model," Phys. Rev. A **79**, 042319 (2009). DOI: 10.1103/PhysRevA.79.042319.

[115] W. Li, Z. Zhang, and P. Tong, "Effect of the Dzyaloshinskii–Moriya interaction on heat conductivity in one-dimensional quantum Ising chains," Eur. Phys. J. B **85**, 73 (2012). DOI: 10.1140/epjb/e2012-20798-6.

[116] One-dimensional quantum spin chains GabrielT.Landi UniversityofS˜ aoPaulo November29,2019

[117] J. C. Bonner and M. E. Fisher, Linear magnetic chains with anisotropic coupling, *Phys. Rev.* **135** (1964) A640–A658.

[118] R. Schmidt and M. Luban, Specific heat of finite spin systems, *Phys. Rev. B* **68** (2003) 184401.

[119] M. O. Scully, M. S. Zubairy, G. S. Agarwal, and H. Walther, Extracting work from a single heat bath via quantum coherence, *Science* **299** (2003) 862–864.

[120] R. Uzdin, A. Levy, and R. Kosloff, Equivalence of quantum heat machines, and quantum-thermodynamic signatures, *Phys. Rev. X* **5** (2015) 031044.

[121] H. T. Quan, Y. X. Liu, C. P. Sun, and F. Nori, Quantum thermodynamic cycles and quantum heat engines, *Phys. Rev. E* **76** (2007) 031105.

[122] J. Gemmer, M. Michel, and G. Mahler, *Quantum Thermodynamics: Emergence of Thermodynamic Behavior Within Composite Quantum Systems*, 2nd ed., Springer, 2009.

[123] I. Affleck, Quantum spin chains and the Haldane gap, *J. Phys. Condens. Matter* **1** (1989) 3047–3072.

[124] F. C. Alcaraz, M. N. Barber, and M. T. Batchelor, Conformal invariance, the XXZ chain, and the operator content of two-dimensional critical systems, *Ann. Phys.* **182** (1987) 280–343.

[125] K. Binder, Finite size scaling analysis of Ising model block distribution functions, *Z. Phys. B* **61** (1985) 13–23.

[126] A. Solfanelli, G. Giachetti, M. Campisi, S. Ruffo and N. Defenu, "Quantum heat engine with long-range advantages," New J. Phys. **25** (2023) 033030.

[127] M. Campisi, P. Talkner, and P. Hänggi, Colloquium: Quantum fluctuation relations: Foundations and applications, *Rev. Mod. Phys.* **83** (2011) 771–791.

[128] Landau, L. D., 1932. On the theory of transfer of energy at collisions II. *Phys. Z. Sowjetunion*, 2, 46.

[129] Zener, C., 1932. Non-adiabatic crossing of energy levels. *Proc. R. Soc. Lond. A*, 137, 696–702.

[130] Guery-Odelin D, Ruschhaupt A, Kiely A, Torrontegui E, Mart´ınez-Garaot S and Muga J 2019 Rev. Mod. Phys. 91 045001 URL https://doi.org/10.1103/RevModPhys.91.045001
[131] Hartmann A, Mukherjee V, Niedenzu W and Lechner W 2020 Phys. Rev. Res. 2 023145 URL https://doi.org/10.1103/PhysRevResearch.2.023145
[132] Cavina V, Mari A, Carlini A and Giovannetti V 2018 Phys. Rev. A 98 012139 URL https://doi.org/10.1103/PhysRevA.98.012139
[133] Suri N, Binder F C, Muralidharan B and Vinjanampathy S 2018 Eur. Phys. J. Spec. Top. 227 203 URL https://doi.org/10.1140/epjst/e2018-00125-6
[134] A E P and No´e F 2022 npj Quantum Inf. 8 1 URL https://doi.org/10.1038/ s41534-021-00512-0
[135] Holubec V and Ryabov A 2017 Phys. Rev. E 96 030102(R) URL https://doi.org/10.1103/ PhysRevE.96.030102
[136] Denzler T and Lutz E 2020 Phys. Rev. Res. 2 032062(R) URL https://doi.org/10.1103/ PhysRevResearch.2.032062
[137] Denzler T and Lutz E 2021 New J. Phys. 23 075003 URL https://doi.org/10.1088/1367-2630/ ac09fe
[138] Myers N M and Deffner S 2020 Phys. Rev. E 101 012110 URL https://doi.org/10.1103/ PhysRevE.101.012110
[139] Zheng Y and Poletti D 2015 Phys. Rev. E 92(1) 012110 URL https://link.aps.org/doi/10. 1103/PhysRevE.92.012110
[140] Zhuan Zhao.Characterizing quantum criticality and steered coherence in the XY-Gamma chain.Phys. Rev. A 105, 063306 – Published 8 June, (2022). DOI:https://doi.org/10.1103/PhysRevA.105.063306
[141] J. Dziarmaga, "Dynamics of a quantum phase transition and relaxation to a steady state," Adv. Phys. **59**(6), 1063–1189 (2010).
[142] L. D. Landau, "Zur Theorie der Energieübertragung II," Z. Sowjetunion **2**, 46 (1932).
[143] C. Zener and R. H. Fowler, "Non-adiabatic crossing of energy levels," Proc. R. Soc. A **137**, 696 (1932).
[144] E. C. G. Stueckelberg, "Theorie der unelastischen stösse zwischen Atomen," Helv. Phys. Acta **5**, 369 (1932).
[145] E. Majorana, "Atomi orientati in campo magnetico variabile," Nuovo Cimento **9**, 43 (1932).
[146] N. V. Vitanov and B. M. Garraway, "Landau–Zener model: effects of finite coupling duration," Phys. Rev. A **53**, 4288 (1996).
[147] C. De Grandi and A. Polkovnikov, "Adiabatic perturbation theory: from Landau–Zener problem to quenching through a quantum critical point," in *Quantum Quenching, Annealing and Computation*, A. K. Chandra, A. Das, and B. K. Chakrabarti (eds.), Springer, Berlin, pp. 75–114 (2010).